*lubricants*

MDPI

*Article*

# Decoupling the Effects of Shear Thinning and Thermal Softening on EHL Film Thickness and Friction

**Rayan Ajeeb, Marko Polajnar and Mitjan Kalin ***

University of Ljubljana, Faculty of Mechanical Engineering Laboratory for Tribology and Interface Nanotechnology, Bogišićeva 8, 1000 Ljubljana, Slovenia; rayan.ajeeb@fs.uni-lj.si (R.A.); marko.polajnar@fs.uni-lj.si (M.P.)
* Correspondence: mitjan.kalin@fs.uni-lj.si

**Abstract**

In elastohydrodynamic lubrication (EHL) contacts, lubricant viscosity plays an important role in friction and film formation. Previous studies have established that shear thinning and thermal softening influence both friction and film thickness. However, the distinct effects of temperature- and shear-rate-dependent viscosity on local cross-film lubricant flow and their relationship to changes in film thickness at high slide-to-roll ratios (SRRs) remain insufficiently resolved. A validated full Navier–Stokes thermo-EHL line-contact model with three viscosity formulations was employed to distinguish the effects of shear thinning and thermal softening on friction, film thickness, and local lubricant flow: (i) a thermal shear-thinning (non-Newtonian) formulation, (ii) a thermal Newtonian formulation, and (iii) a thermally uncoupled shear-thinning (isothermal non-Newtonian) formulation. Two parameter sweeps were performed: the slide-to-roll ratio (SRR) was varied at a fixed entrainment velocity, and the entrainment velocity was varied at a fixed SRR. With increasing sliding speed, thermal softening becomes more important for friction behaviour relative to shear thinning, resulting in the transition from shear-thinning-dominated to thermal-softening-dominated friction behaviour. Similarly, thermal softening has a greater influence on film thickness than shear thinning. Shear thinning primarily reduces viscosity and wall shear stress while maintaining a nearly linear Couette-type velocity profile, with only a minor effect on film thickness. In contrast, an important new phenomenon is that thermal softening has a distinct effect on film thickness. When the contacting surfaces move at different velocities, thermal softening produces a non-uniform cross-film viscosity distribution, which redistributes the velocity gradient and increases the mean lubricant velocity. For a given mass flow, this increase in mean velocity reduces film thickness, consistent with the conservation of mass.

**Keywords:** elastohydrodynamic lubrication; shear thinning; thermal softening; coefficient of friction; film thickness; Navier–Stokes modelling

Received: 7 September 2026
Revised: 22 October 2026
Accepted: 27 October 2026
Published: 30 October 2026

**Copyright:** © 2026 by the authors. Licensee MDPI, Basel, Switzerland. This article is an open access article distributed under the terms and conditions of the Creative Commons Attribution (CC BY) license.

## 1. Introduction

Elastohydrodynamic lubrication (EHL) occurs in highly loaded non-conformal contacts, such as rolling bearings, gears, cam–follower systems, and friction drives [1–3]. High fluid pressure deforms the contacting solids elastically and increases lubricant viscosity, allowing a thin lubricant film to support severe normal loads [4,5].

Sliding in EHL contacts induces viscous shear within the lubricant film [6–11]. The resulting shear stresses and shear rates produce viscous friction, which generates heat

within the lubricant. Frictional heating increases the lubricant temperature and consequently reduces its local viscosity. This temperature-induced viscosity reduction [12,13] is referred to as thermal softening [14–19]. At the same time, severe shear stresses and shear rates cause many lubricants to exhibit a nonlinear shear response [7,9,20–23]. Under sufficiently high shear, their effective viscosity also decreases. This behaviour is known as shear thinning. Thermal softening and shear thinning are therefore two distinct mechanisms that can occur simultaneously in EHL contacts. Both mechanisms reduce lubricant viscosity and, consequently, EHL friction.

At a given local shear rate, shear thinning reduces shear stress compared with Newtonian behaviour and consequently decreases local viscous heat generation. This can reduce the temperature rise and weaken thermal softening. Conversely, temperature-induced viscosity changes can modify the local shear stress and shear rate distributions, thereby affecting the shear-thinning response. Thus, the two mechanisms influence each other. Both mechanisms should therefore be considered when their effects are significant under the operating conditions investigated. Thermal softening is commonly represented using pressure- and temperature-dependent viscosity relations, such as Roelands-type formulations [24–26] or free-volume-based Yasutomi relations [27,28]. Shear thinning is described using non-Newtonian constitutive models, including the commonly employed Eyring [21,29] and Carreau [30] models [31–34].

The influence of shear thinning and thermal softening on friction in EHL has been extensively investigated. Habchi et al. [10] investigated EHL friction as a function of the slide-to-roll ratio (SRR) at a fixed entrainment speed and identified four friction regimes. At low SRRs, friction increased almost linearly with the SRR. As the SRR increased, shear thinning became important, and the friction response became nonlinear. At intermediate SRRs, friction could reach a plateau associated with limiting shear stress. At higher SRRs, viscous heating became more important, leading to a thermo-viscous response in which shear thinning remained active. MacLaren and Kadiric [11] experimentally observed a similar transition from shear-thinning-dominated behaviour at intermediate SRRs to thermally dominated behaviour at high SRRs. In the shear-thinning-dominated region, they also observed an Eyring-type relationship between shear stress and shear rate [11]. Together, these studies showed that the friction response is nearly Newtonian at low shear rates, becomes increasingly influenced by shear thinning at intermediate shear rates, and is more strongly affected by thermal softening at high shear rates.

Regarding film thickness, several studies have reported reductions caused by shear thinning. Liu et al. [8] showed that their numerical EHL model accurately predicted measured film thickness when shear thinning was included, whereas neglecting shear thinning led to overprediction. Katyal and Kumar [35] further showed that this reduction can occur even under pure rolling conditions because shear thinning can develop in the inlet without sliding between the contacting surfaces. More recently, Bair and Habchi [22] investigated a mildly shear-thinning lubricant in rolling line contacts. They found that even mild shear thinning in the inlet can change film thickness predictions and their dependence on operating conditions. These studies established that shear thinning can reduce film thickness, but its influence depends on the lubricant properties and the operating conditions.

Other studies have attributed film thickness reduction to thermal softening. Kumar and Khonsari [9] investigated the combined effects of viscous heating and shear thinning in rolling/sliding EHL line contacts. They showed that thermal effects influence film thickness and that the response depends on the lubricant's shear-thinning properties. MacLaren and Kadiric [11] subsequently measured film thickness at high entrainment speeds and found lower values than those predicted by conventional isothermal EHL models. They attributed this reduction to lubricant heating in the inlet, including heat transferred from the contacting solids. He et al. [36] used a thermal EHL model of gear

contacts and predicted thinner films than conventional analytical models. They partly attributed this difference to sliding-induced heating, which reduces lubricant viscosity. These studies showed that thermal effects can also reduce EHL film thickness.

Since shear thinning and thermal softening can occur simultaneously in EHL contacts, distinguishing their effects is important for understanding the resulting film thickness response. Previous studies have attempted to separate these effects. Kumar and Khonsari [9] compared Newtonian and shear-thinning formulations while accounting for viscous heating and showed that the thermal influence on film thickness depended on the lubricant's shear-thinning properties. Echávarri et al. [37] used separate correction factors for inlet shear heating and shear thinning to calculate central film thickness. De la Guerra et al. [38] subsequently evaluated shear-thinning film thickness corrections under isothermal conditions and thermal corrections separately before combining them. Their combined predictions showed a reduction in film thickness with an increasing SRR. These studies demonstrated that distinguishing the two effects provides important information for predicting EHL film thickness.

Previous studies have established that both shear thinning and thermal softening can influence EHL friction and film thickness and have developed several approaches to distinguish their effects. However, the correction-factor approaches of Echávarri et al. [37] and de la Guerra et al. [38] do not directly compare how the temperature and shear-rate dependencies of viscosity separately modify the local lubricant flow and the resulting film thickness under identical operating conditions. In particular, these approaches do not provide spatially resolved comparisons of the cross-film velocity distributions associated with the two mechanisms at high SRRs.

The present study addresses this mechanistic question through three viscosity formulations within the same validated EHL framework. These comprise a thermal shear-thinning (non-Newtonian) formulation accounting for both shear thinning and thermal softening; a thermal Newtonian formulation accounting for thermal softening; and a thermally uncoupled shear-thinning (isothermal non-Newtonian) formulation accounting for shear thinning. The full Navier–Stokes EHL formulation was selected because it directly resolves the local cross-film velocity, temperature, and viscosity fields within the coupled solution. This controlled comparison allows the effects of shear thinning and thermal softening on friction, film thickness, and local lubricant flow to be examined under otherwise identical operating conditions. The comparison is performed over a range of SRRs and entrainment velocities. A limited additional comparison of key mechanisms using alternative shear-thinning (Eyring and modified Carreau–Yasuda) and pressure–temperature viscosity (Roelands and Vogel-like) formulations is also presented.

The remainder of this paper is organized as follows. Section 2 presents the numerical methodology; Section 3 reports the results; Section 4 discusses the underlying physical mechanisms; and Section 5 summarizes the main conclusions.

## 2. Numerical Methodology

### *2.1. Computational Model*

The full Navier–Stokes formulation was selected to distinguish between thermal and shear effects on local viscosity fields, together with velocities and corresponding temperature profiles. The present analysis therefore specifically examines the redistribution of the local cross-film velocity, temperature, and viscosity fields. With point-by-point field resolution across the fluid domain, velocity is solved locally from the momentum equations, and, for the thermal formulations, temperature is solved from the energy equation, while viscosity is evaluated locally from the corresponding pressure, temperature, and shear rate conditions. This local field resolution allows temperature- and shear-dependent

viscosity changes to be related directly to lubricant flow, wall shear stress, and film thickness response [39].

The model was implemented in ANSYS Fluent 2024 (ANSYS, Inc., Canonsburg, PA, USA) using the finite volume method and the coupled pressure–velocity algorithm. User-defined functions (UDFs) were employed for the viscosity and density relations, the heat-source treatment, and the thermal boundary conditions, and the vertical displacement of the flat surface was used for load balancing. The model combines cavitation, elastic deformation, and iterative thermal coupling between the lubricant and the contacting solids.

As shown in Figure 1, the EHL conjunction consists of a thin lubricant film confined between a cylindrical surface and a flat surface, representing the contact geometry encountered in cylindrical rolling bearings, gears, and cam–follower mechanisms [40]. The cylinder diameter is 20 mm, while the total computational length in the entrainment direction is 7 mm. The domain extends well beyond the Hertzian contact region, allowing the inlet film to develop before the contact and the pressure to relax within the outlet region. For the applied load of 100 $\mathrm{kN \cdot m^{-1}}$, the corresponding Hertzian contact half-width is $a = 105$ μm. This load and contact geometry thus result in a maximum Hertzian contact pressure of 0.61 GPa.

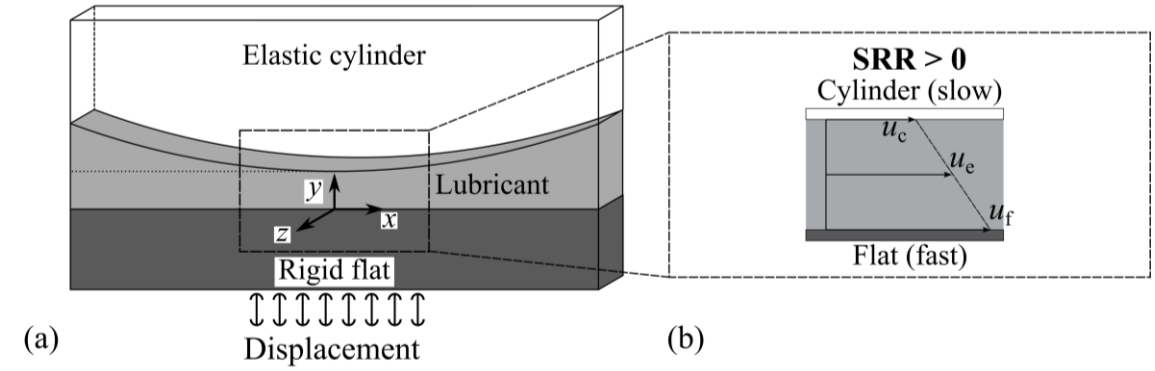



**Figure 1.** (**a**) Schematic of the computational domain used for the EHL line-contact model. (**b**) Schematic illustration of entrainment velocity $(u_e)$ and surface velocities of the cylinder $(u_c)$ and flat $(u_f)$ for positive slide-to-roll ratios (SRR > 0).

The computational model shown in Figure 1a represents an EHL line contact. However, the coupled fluid–solid solution was implemented using a thin three-dimensional slice containing one computational cell in the transverse direction. This pseudo-two-dimensional representation provides a surface for transferring pressure and displacement between the fluid and solid domains while preserving the physical interpretation of a two-dimensional line contact.

The deformable upper solid was modelled as a truncated cylinder with a height of 2 mm, measured from the lubricant–solid interface to the upper solid boundary at the contact centre. This dimension was selected to minimize the influence of remote boundary constraints on the contact-induced elastic deformation.

The tangential velocities of the cylindrical and flat surfaces are denoted by $u_c$ and $u_f$, respectively. The entrainment velocity is defined as:

$$u_e = \frac{u_f + u_c}{2}, \quad (1)$$

and the slide-to-roll ratio (SRR) is defined as:

$$\mathrm{SRR} = \frac{u_f - u_c}{u_e}. \quad (2)$$

Non-negative SRR values were considered. For SRR > 0, the lower flat surface was faster than the upper cylinder surface; at SRR = 0, their velocities were equal.

Two sets of simulations were performed: slide-to-roll ratio variation and entrainment velocity variation. The slide-to-roll ratio variation simulations used a constant entrainment velocity of 2.5 m $s^{-1}$, while SRR was varied systematically from 0 to 1.5 to modify the sliding velocity, shear rate, and heat generation without changing the prescribed entrainment velocity. The entrainment velocity variation simulations used a fixed positive SRR of 1.5, while the entrainment velocity was varied from 0.5 to 2.5 m $s^{-1}$. The coefficient of friction (COF) on the flat surface was defined as:

$$\mathrm{COF} = \frac{\left|\int_{x_{\mathrm{in}}}^{x_{\mathrm{out}}} \tau_{\mathrm{w}}(x)\, dx\right|}{\int_{x_{\mathrm{in}}}^{x_{\mathrm{out}}} p(x)\, dx}. \quad (3)$$

Atmospheric pressure was prescribed at the fluid inlet and outlet. A symmetry boundary condition was applied to the side fluid walls to enforce zero normal gradients of flow and thermal variables. The cylinder velocity ($u_c$) was imposed at the upper fluid–solid interface, while the flat surface velocity ($u_f$) was imposed at the lower interface [Figure 1a]. The lower flat surface was allowed to move in the normal direction to adjust the lubricant film separation until the prescribed normal load was achieved.

The upper boundary of the deformable solid was fixed, whereas its lateral boundaries were restricted in the normal direction. Pressure loads were transferred from the lubricant to the deformable solid, and the resulting interfacial displacements were returned to the fluid domain through two-way fluid–structure interaction.

The solid properties correspond to those of AISI 52100 steel. The lubricant properties were selected from values reported in the EHL and TEHL literature [39,41,42]. The ambient viscosity (0.01 Pa·s), reference density (850 kg·$m^{-3}$), and pressure–viscosity coefficient (17.34 $GPa^{-1}$) are within ranges reported for EHL lubricants [43–45]. The temperature–viscosity coefficient (0.0476 $K^{-1}$), thermal conductivity (0.15 W·$m^{-1}$·$K^{-1}$), specific heat capacity (2300 J·$kg^{-1}$·$K^{-1}$), and volumetric thermal expansion coefficient (4.5 × $10^{-4}$ $K^{-1}$) are supported by previous thermal EHL studies [39,45,46]. An Eyring stress of 5 MPa was selected based on values reported for shear-thinning EHL formulations [20,47]. The resulting property set therefore represents a literature-based reference lubricant and was applied consistently in all three formulations used in the present comparative study. All operating conditions, material properties, and lubricant properties are summarized in Table 1.

### *2.2. Computational Mesh*

A structured mesh was employed in the lubricant domain. As shown in Figure 2, the mesh was highly refined within the Hertzian region to resolve the pressure, velocity, viscosity, shear rate, and temperature gradients.

In the streamwise direction, the domain was discretized using 150 cells in the inlet region, 1000 cells within the refined contact region, and 150 cells in the outlet region. The refined region extended over 1.1 × 2$a$. The lubricant film thickness was discretized using 12 cells.

The internal fluid mesh was updated using spring-based smoothing [48,49]. In this method, the mesh edges are treated as interconnected elastic springs. This approach preserves mesh cell quality during deformation.

**Table 1.** Model-relevant parameters.

| Parameter | Value | Unit |
|---|---|---|
| Cylinder diameter | 20 | [mm] |
| Solid's elastic modulus | 210 | [GPa] |
| Poisson's ratio | 0.3 | / |
| Steel density | 7850 | [kg·m$^{-3}$] |
| Steel specific heat capacity | 450 | [J·kg$^{-1}$·K$^{-1}$] |
| Steel thermal conductivity | 47 | [W·m$^{-1}$·K$^{-1}$] |
| Liquid density | 850 | [kg·m$^{-3}$] |
| Ambient viscosity | 0.01 | [Pa·s] |
| Liquid specific heat capacity | 2300 | [J·kg$^{-1}$·K$^{-1}$] |
| Liquid thermal conductivity | 0.15 | [W·m$^{-1}$·K$^{-1}$] |
| Thermo-viscous constant | 0.0476 | [K$^{-1}$] |
| Volumetric coefficient of thermal expansion | $4.5{\cdot}10^{-4}$ | [K$^{-1}$] |
| Ambient temperature | 353 | [K] |
| Saturation pressure | $5{\cdot}10^{3}$ | [Pa] |
| Vapour density | 0.0288 | [kg·m$^{-3}$] |
| Vapour viscosity | $8.97{\cdot}10^{-6}$ | [Pa·s] |
| Vapour specific heat capacity | 1800 | [J·kg$^{-1}$·K$^{-1}$] |
| Vapour thermal conductivity | 0.025 | [W·m$^{-1}$·K$^{-1}$] |
| Pressure–viscosity coefficient | 17.34 | [GPa$^{-1}$] |
| Eyring stress | 5 | [MPa] |
| Entrainment velocity | 2.5 m/s for SRR variation; 0.5–2.5 m/s for $u_e$ variation | [m·s$^{-1}$] |
| SRR | 0–1.5 for SRR variation; 1.5 for $u_e$ variation | |
| Load per unit length | 100 | [kN·m$^{-1}$] |
| Hertzian contact half-width | 105 | [μm] |

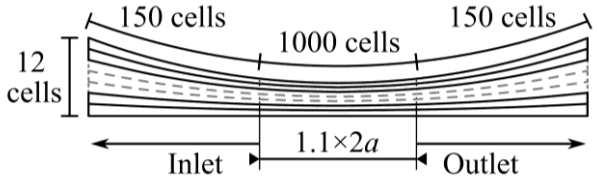



**Figure 2.** Schematic of the computational mesh. The refined region spans 1.1 × 2a and is discretized with 1000 cells. The inlet and outlet regions use 150 cells each. The film thickness is discretized with 12 cells.

### *2.3. Viscosity Formulations*

Three viscosity formulations were implemented to examine the effects of shear thinning and thermal softening on friction and film thickness under otherwise identical operating conditions. The Roelands relation [50] was adopted to describe pressure- and temperature-dependent viscosity as one of the most frequently used models in EHL and TEHL [24–26]. Of the two commonly used approaches for shear-thinning behaviour [31–34,51–56], namely, Eyring [21,29] and Carreau [30], the Eyring formulation was selected [21,29]. Although a comprehensive investigation of the influence of different shear-thinning and thermal softening models is beyond the scope of this work, the selection of these models may influence the results and conclusions of the study. Accordingly, additional analyses were performed using the modified Carreau–Yasuda [57] and Vogel-like thermodynamic scaling [58] formulations for a different, well-characterised lubricant (Shell T9) [59]. A limited set of key results is presented to examine whether the identified

physical mechanisms remain consistent when using different rheological formulations and lubricant properties.

Based on these relations, three viscosity formulations were defined by purposely including or excluding the effects of temperature and shear rate, as summarized in Table 2.

**Table 2.** Comparison of the three viscosity formulations.

| Viscosity Formulation | Pressure Dependence | Thermal Softening | Shear Thinning |
|---|---|---|---|
| Thermal Newtonian, $[\eta(p,T)]$ | Yes | Yes | No |
| Isothermal non-Newtonian, $[\eta(p,\dot{\gamma})]$ | Yes | No | Yes |
| Thermal non-Newtonian, $[\eta(p,T,\dot{\gamma})]$ | Yes | Yes | Yes |

2.3.1. Thermal Newtonian Formulation $[\eta(p,T)]$

The lubricant was assumed to behave as a Newtonian fluid (with shear thinning excluded), and the viscosity was considered a function of both pressure and temperature. The pressure- and temperature-dependent viscosity was calculated using the Roelands equation [50]:

$$\eta_{\text{eff}} = \eta(p,T) = \eta_0 \exp\left\{[\ln(\eta_0) + 9.67]\left[-1 + C(p)\left(\frac{T-138}{T_0-138}\right)^{-S_0}\right]\right\}, \quad (4)$$

where

$$Z = \frac{\alpha}{5.1\times10^{-9}[\ln(\eta_0)+9.67]}, C(p) = (1+5.1\times10^{-9}p)^Z, \text{and } S_0 = \frac{\beta(T_0-138)}{\ln(\eta_0)+9.67}. \quad (5)$$

2.3.2. Isothermal Shear-Thinning Formulation $[\eta(p,\dot{\gamma})]$

The lubricant viscosity was assumed to depend on pressure and shear rate, while the effect of temperature (thermal softening) was neglected. First, the pressure-dependent Newtonian viscosity was determined from the Roelands equation [50]:

$$\eta_{\text{R}}(p) = \eta_0 \exp\{[\ln(\eta_0) + 9.67][-1 + C(p)]\}. \quad (6)$$

Equation (6) is then used in the Eyring model [21,29] to calculate the effective viscosity:

$$\eta_{\text{eff}} = \eta(p,\dot{\gamma}) = \begin{cases} \eta_{\text{R}}(p), & \dot{\gamma} < \dot{\gamma}_{\min}, \\ \frac{\tau_0}{\dot{\gamma}}\sinh^{-1}\left(\frac{\eta_R(p)\dot{\gamma}}{\tau_0}\right), & \dot{\gamma} \geq \dot{\gamma}_{\min}. \end{cases} \quad (7)$$

2.3.3. Thermal Shear-Thinning Formulation $[\eta(p,T,\dot{\gamma})]$

The lubricant viscosity depends on pressure, temperature, and shear rate. The pressure- and temperature-dependent viscosity is first evaluated using the Roelands equation [50]:

$$\eta_{\text{R}}(p,T) = \eta_0 \exp\left\{[\ln(\eta_0) + 9.67]\left[-1 + C(p)\left(\frac{T-138}{T_0-138}\right)^{-S_0}\right]\right\}. \quad (8)$$

Equation (8) is then used in the Eyring model [21,29]:

$$\eta_{\text{eff}} = \eta(p,T,\dot{\gamma}) = \begin{cases} \eta_{\text{R}}(p,T), & \dot{\gamma} < \dot{\gamma}_{\min}, \\ \dfrac{\tau_0}{\dot{\gamma}} \sinh^{-1}\left(\dfrac{\eta_{\text{R}}(p,T)\dot{\gamma}}{\tau_0}\right), & \dot{\gamma} \geq \dot{\gamma}_{\min}. \end{cases} \quad (9)$$

The cutoff $\dot{\gamma}_{\min}$ in Equations (7) and (9) was introduced only to avoid numerical indeterminacy as $\dot{\gamma} \to 0$. Following Hartinger et al. [25], the numerical cutoff was set to $\dot{\gamma}_{\min} = 10^{-8}\text{s}^{-1}$.

### *2.4. Fluid Governing Equations*

The lubricant and vapour phases coexist within the fluid domain and are represented by their local volume fractions, with:

$$\alpha_{\text{l}} + \alpha_{\text{v}} = 1, \quad (10)$$

where $\alpha_{\text{l}}$ and $\alpha_{\text{v}}$ are the liquid and vapour volume fractions. The mixture properties used in the governing equations were evaluated locally from the liquid and vapour volume fractions and their respective material properties. The liquid lubricant predominates in the inlet and pressurized contact regions. Cavitation is treated using the Schnerr–Sauer model [60], with the liquid lubricant defined as the primary phase and vapour as the secondary phase. When the local pressure decreases below the prescribed saturation pressure, evaporation transfers mass from the liquid to the vapour phase; when the pressure recovers above the saturation condition, condensation transfers mass back to the liquid phase. Atmospheric pressure is prescribed at both the fluid inlet and outlet, while the saturation pressure is $p_{sat} = 5000$ Pa (Table 1). The cavitation treatment is retained to provide a physically consistent description of the diverging outlet region; cavitation itself is not the mechanism investigated in the present comparative study. Mass conservation is governed by:

$$\frac{\partial \rho_{\text{m}}}{\partial t} + \nabla \cdot (\rho_{\text{m}} \mathbf{u}_{\text{m}}) = 0. \quad (11)$$

The mixture momentum equation of the liquid and vapour phases is written as:

$$\frac{\partial (\rho_{\text{m}} \mathbf{u}_{\text{m}})}{\partial t} + \nabla \cdot (\rho_{\text{m}} \mathbf{u}_{\text{m}} \otimes \mathbf{u}_{\text{m}}) = -\nabla p + \nabla \cdot \boldsymbol{\sigma}_{\text{f}}. \quad (12)$$

### *2.5. Thermal Energy Equation*

For the thermal Newtonian $[\eta(p,T)]$ and thermal shear-thinning (non-Newtonian) $[\eta(p,T,\dot{\gamma})]$ formulations, the lubricant temperature was obtained from the energy equation. Heat generation arises from viscous dissipation and compressive work [61]. The steady-state energy balance is expressed as:

$$\rho_{\text{m}} c_{p,\,\text{m}} (\mathbf{u}_{\text{m}} \cdot \nabla T) = \nabla \cdot (k_{\text{m}} \nabla T) + Q_{\text{shear}} + Q_{\text{comp}}, \quad (13)$$

where $Q_{\text{shear}}$ and $Q_{\text{comp}}$ represent heating due to viscous shear [62] and compressive work [63], respectively. They are defined as [64]:

$$Q_{\text{shear}} = \eta_{\text{eff}} \left( \nabla \mathbf{u}_{\text{m}} : \nabla \mathbf{u}_{\text{m}} + \nabla \mathbf{u}_{\text{m}} : (\nabla \mathbf{u}_{\text{m}})^T - \frac{2}{3} (\nabla \cdot \mathbf{u}_{\text{m}})^2 \right), \quad (14)$$

$$Q_{\text{comp}} = -\frac{T}{\rho_{\text{m}}} \left( \frac{\partial \rho_{\text{m}}}{\partial T} \right) (\mathbf{u}_{\text{m}} \cdot \nabla p). \quad (15)$$

Shear heating is expected to be strongest within the highly sheared contact region, whereas compressive heating is associated mainly with lubricant pressurization in the inlet region. For the thermally uncoupled shear-thinning (isothermal non-Newtonian) formulation, Equation (13) was not solved, and the lubricant temperature was maintained at the reference value $T_0$.

### *2.6. Density*

In all three formulations, the lubricant density was considered pressure-dependent only and was calculated as [65]:

$$\rho_l(p) = \rho_0 \left(1 + \frac{0.59\times10^{-9}\cdot p}{1+1.7\times10^{-9}\cdot p}\right). \quad (16)$$

Temperature dependence of density was deliberately omitted so that the comparison isolates the effects of the three viscosity formulations described in Section 2.3.

### *2.7. Thermal Boundary Treatment*

At each fluid–solid interface, the heat flux transferred from the lubricant to the solid was calculated from the near-wall temperature gradient:

$$\hat{q}_f(\hat{s}) = -k_f \nabla T_f \cdot \mathbf{n}, \quad (17)$$

where $\mathbf{n}$ is the outward unit normal from the fluid domain and s denotes the streamwise integration coordinate. The resulting solid surface temperature was determined using the Carslaw–Jaeger moving heat-source solution for a semi-infinite body [66,67]:

$$T_s(s) = T_0 + \frac{1}{\sqrt{\pi \rho_s c_{p,s} k_s u_s}} \int_{-\infty}^{s} \frac{\hat{q}_f(\hat{s})}{\sqrt{s-\hat{s}}} d\hat{s}, \quad (18)$$

where $u_s$ is the local surface speed. Equation (18) was evaluated separately for the two moving surfaces using their respective velocities and interfacial heat flux distributions. The calculated surface temperatures were then imposed as the thermal boundary conditions of the lubricant domain.

This procedure closes the thermal feedback loop between the lubricant and the solids. Viscous and compressive heating within the fluid domain modify the interfacial heat flux. The resulting heat flux changes the solid–fluid interface temperatures and hence the lubricant temperature. This, in turn, modifies the lubricant viscosity, shear stress, and subsequent heat generation.

The thermal boundary solver was activated in the thermal formulations. In the isothermal formulation, both fluid–solid interfaces and the lubricant were maintained at $T_0$.

### *2.8. Solid*

The contacting solids were assumed to be homogeneous, isotropic, and linearly elastic. Structural inertia was neglected, and the solid deformation was obtained from the static equilibrium equation [68]:

$$\nabla \cdot \boldsymbol{\sigma}_s = \nabla \cdot (\mathbf{C} \cdot \boldsymbol{\varepsilon}) = 0. \quad (19)$$

Following the reduced one-body formulation presented by Habchi [64,69], the total elastic deformation of the two contacting bodies was assigned to the cylindrical solid, while the flat surface was treated as rigid. The reduced elastic properties satisfy [64]:

$$\frac{1-\nu_{rc}^2}{E_{rc}} = \frac{1-\nu_{steel}^2}{E_{steel}} + \frac{1-\nu_{steel}^2}{E_{steel}}. \quad (20)$$

For two identical steel bodies $(E_1 = E_2 = E_{steel}, \nu_1 = \nu_2 = \nu_{steel})$, this gives [64]:

$$E_{rc} = \frac{E_{steel}}{2} \text{ and } \nu_{rc} = \nu_{steel}. \quad (21)$$

The reduced radius is defined by:

$$\frac{1}{R_{rc}} = \frac{1}{R_1} + \frac{1}{R_2}. \quad (22)$$

### *2.9. Numerical Solution Procedure*

The coupled numerical procedure is presented in Figure 3. The procedure was initiated from the undeformed geometry with a predefined initial film thickness. The fluid and solid domains were coupled through a strong two-way fluid–structure interaction. For each SRR and model configuration, the following sequence was applied:

1. The continuity and momentum equations were solved in the fluid domain for the current film geometry.
2. For the thermal formulations, the fluid energy equation was solved, and the Carslaw–Jaeger thermal boundary solver was applied.
3. The pressure distribution and local normal load were calculated.
4. The local fluid-generated load at the interface was transferred to the deformable solid.
5. The solid equilibrium equation was solved to obtain elastic surface displacement.
6. The displacement was transferred back to the fluid domain, and the dynamic mesh was updated.
7. The vertical position of the flat surface was adjusted according to the difference between the calculated and target loads.
8. The coupled sequence was repeated until the pressure, film thickness, temperature, COF, and normal load reached steady values.

The applied load per unit length was calculated by integrating the hydrodynamic pressure over the contact:

$$W' = \int_{x_{\mathrm{in}}}^{x_{\mathrm{out}}} p\,(x)\,dx \tag{23}$$

Load convergence was defined by a relative difference of less than 0.001% between the calculated and target loads, maintained for 200 consecutive coupling iterations.

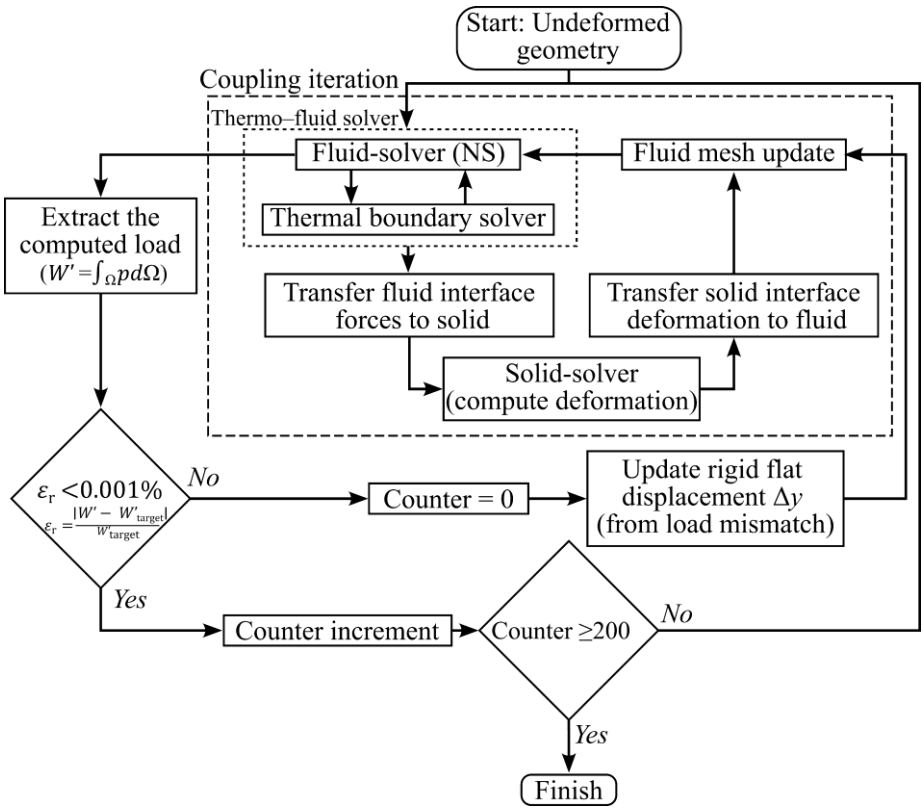



**Figure 3.** Flowchart of the coupled thermo–fluid–solid solution procedure used for the three EHL model configurations.

### *2.10. Model Validation*

To assess the accuracy of the model and its numerical solution procedure, the model was validated under isothermal and thermal EHL conditions. The isothermal validation was used to assess the pressure, elastic deformation, and film thickness predictions, whereas the thermal validation additionally assessed the energy equation and the thermal coupling between the lubricant and contacting solids. The validation results are presented in Appendix A.1 for the isothermal model and Appendix A.2 for the thermal model.

The results in Figure A1 show that the predicted pressure distribution and film thickness profile agree closely with both reference solutions. The agreement confirms the ability of the isothermal model to reproduce the pressure generation, elastic deformation, and film formation of an isothermal EHL line contact.

The results in Figure A2 show that the thermal model reproduces pressure and film thickness distributions closely, showing that the coupled hydrodynamic, elastic, and thermal solution reproduces the principal characteristics of the reference case. In addition to the pressure and film thickness agreement, the predicted maximum temperature rise was $\Delta T_{\max} = 14.83$ K, in agreement with Hartinger's reported temperature rise of up to 15 K for the corresponding thermal EHL case. The agreement in pressure, film thickness, and maximum temperature rise supports the implementation of the fluid energy equation and the thermal coupling between the lubricant and the contacting solids.

### *2.11. Deviation in the Coefficient of Friction and Normalized Parameters*

To quantify the relative influence of shear thinning and thermal softening on friction, the deviations in the coefficient of friction associated with these two effects are reported below. The deviation in the coefficient of friction associated with shear thinning was defined as:

$$D_{\dot{\gamma}}^{(\mathrm{COF})} = \frac{|\ \mathrm{COF}_{p,T} - \mathrm{COF}_{p,T,\dot{\gamma}}\ |}{\mathrm{COF}_{p,T,\dot{\gamma}}} \times 100\% \tag{24}$$

The deviation in the coefficient of friction associated with thermal softening was defined as:

$$D_{T}^{(\mathrm{COF})} = \frac{|\ \mathrm{COF}_{p,\dot{\gamma}} - \mathrm{COF}_{p,T,\dot{\gamma}}\ |}{\mathrm{COF}_{p,T,\dot{\gamma}}} \times 100\% \tag{25}$$

The thermal shear-thinning (non-Newtonian) formulation $[\eta(p,T,\dot{\gamma})]$ was selected as the reference because it includes all viscosity dependencies considered here. The deviations therefore quantify the relative change from the thermal shear-thinning (non-Newtonian) formulation prediction caused by omitting one dependence while retaining the others.

Cross-film temperature, viscosity, and velocity profiles are presented using normalized film thickness and velocity. The cross-film coordinate representing the lubricant film thickness was normalized as:

$$y^* = \frac{y}{h} \tag{26}$$

where $y^* = 0$ corresponds to the flat surface and $y^* = 1$ corresponds to the cylindrical surface. The velocity was normalized as:

$$u^* = \frac{u - u_{\mathrm{f}}}{u_{\mathrm{c}} - u_{\mathrm{f}}} \tag{27}$$

Under ideal Couette flow, the corresponding normalized profile is $u^* = y^*$.

## 3. Results

### *3.1. Slide-to-Roll Ratio Variation*

The first set of simulations was performed at a constant entrainment velocity of $u_e = 2.5\ \mathrm{m\,s^{-1}}$ while the slide-to-roll ratio was varied from 0 to 1.5. The three viscosity formulations were compared: the thermal shear-thinning (non-Newtonian) formulation $[\eta(p,T,\dot{\gamma})]$; the thermal Newtonian formulation $[\eta(p,T)]$; and the thermally uncoupled shear-thinning (isothermal non-Newtonian) formulation $[\eta(p,\dot{\gamma})]$.

Figure 4a shows the coefficient of friction as a function of the SRR. As the SRR increases, the predictions of the three formulations diverge from the common zero-friction condition; for the thermal shear-thinning formulation $[\eta(p,T,\dot{\gamma})]$, the coefficient of friction increased to a maximum value of 0.023 at SRR = 0.5. It then decreased to 0.019 at SRR = 1.5.

For the thermal Newtonian formulation $[\eta(p,T)]$, the coefficient of friction increased to a maximum value of 0.036 at SRR = 0.25. It then decreased continuously and reached 0.022 at SRR = 1.5. For the thermally uncoupled shear-thinning (isothermal non-Newtonian) formulation $[\eta(p,\dot{\gamma})]$, the coefficient of friction increased continuously with SRR, reaching 0.042 at SRR = 1.5.

Figure 4b shows the deviations in the COF with respect to the thermal shear-thinning (non-Newtonian) formulation $[\eta(p,T,\dot{\gamma})]$. The COF deviation associated with shear thinning reached its maximum value of 71.3% at SRR = 0.125. It then decreased to 14.8% at SRR = 1.5. The COF deviation associated with thermal softening was 9.2% at SRR = 0.125. It increased monotonically to 119.6% at SRR = 1.5. The two COF-deviation curves crossed at SRR ≈ 0.57, indicating a transition from a shear-thinning-dominated COF to a thermal-softening-dominated COF.

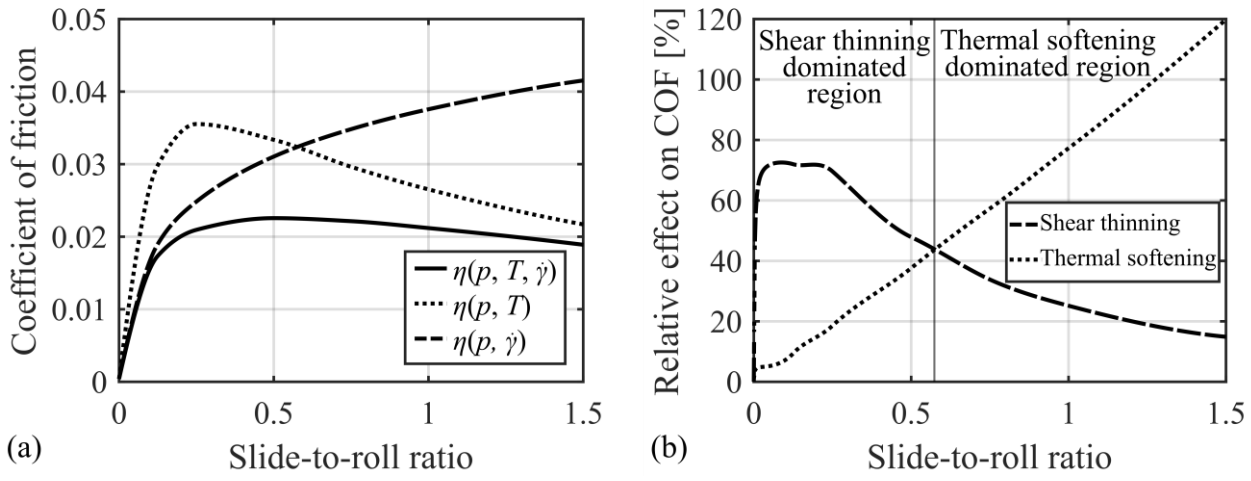



**Figure 4.** (**a**) Variation in the coefficient of friction and (**b**) deviations in the COF associated with shear thinning and thermal softening, evaluated with respect to the thermal shear-thinning (non-Newtonian) formulation $[\eta(p,T,\dot{\gamma})]$, as a function of the SRR at a constant entrainment velocity of 2.5 $\mathrm{m\,s^{-1}}$.

Figure 5a shows the central film thickness as a function of the SRR. For the thermal shear-thinning (non-Newtonian) formulation $[\eta(p,T,\dot{\gamma})]$, the central film thickness decreased from 207 nm at SRR = 0 to 173 nm at SRR = 1.5. For the thermal Newtonian formulation $[\eta(p,T)]$, it decreased with the SRR from 207 nm to 170 nm. For the isothermal non-Newtonian formulation $[\eta(p,\dot{\gamma})]$, it remained nearly constant with values between 208 nm and 209 nm.

Figure 5b shows the variation in the minimum film thickness as a function of the SRR. For the thermal non-Newtonian formulation $[\eta(p,T,\dot{\gamma})]$, the minimum film thickness decreased from 175 nm at $\text{SRR} = 0$ to 147 nm at $\text{SRR} = 1.5$. For the thermal Newtonian formulation $[\eta(p,T)]$, it decreased with the SRR from 175 nm to 146 nm. For the thermally uncoupled shear-thinning (isothermal non-Newtonian) formulation $[\eta(p,\dot{\gamma})]$, it remained nearly constant with values between 174 nm and 177 nm. The difference between both thermal formulations $[\eta(p,T,\dot{\gamma})\ and\ \eta(p,T)]$ and the isothermal formulation $[\eta(p,\dot{\gamma})]$ increased with the SRR, indicating that thermal softening is the dominant film thickness reduction mechanism at high SRRs under the investigated conditions.

Figure 6 shows the maximum lubricant temperature rise $(\Delta T)$ as a function of the SRR. For the thermal shear-thinning (non-Newtonian) formulation $[\eta(p,T,\dot{\gamma})]$, the maximum temperature rise increased from 0.78 K at $\text{SRR} = 0$ to 20.51 K at $\text{SRR} = 1.5$. For the thermal Newtonian formulation $[\eta(p,T)]$, it increased from 0.85 K to 23.74 K. The thermal Newtonian formulation produced a higher maximum temperature rise than the thermal shear-thinning (non-Newtonian) formulation across the full SRR range. For the thermally uncoupled shear-thinning (isothermal non-Newtonian) formulation $[\eta(p,\dot{\gamma})]$, the temperature was prescribed as constant, and no temperature rise took place.

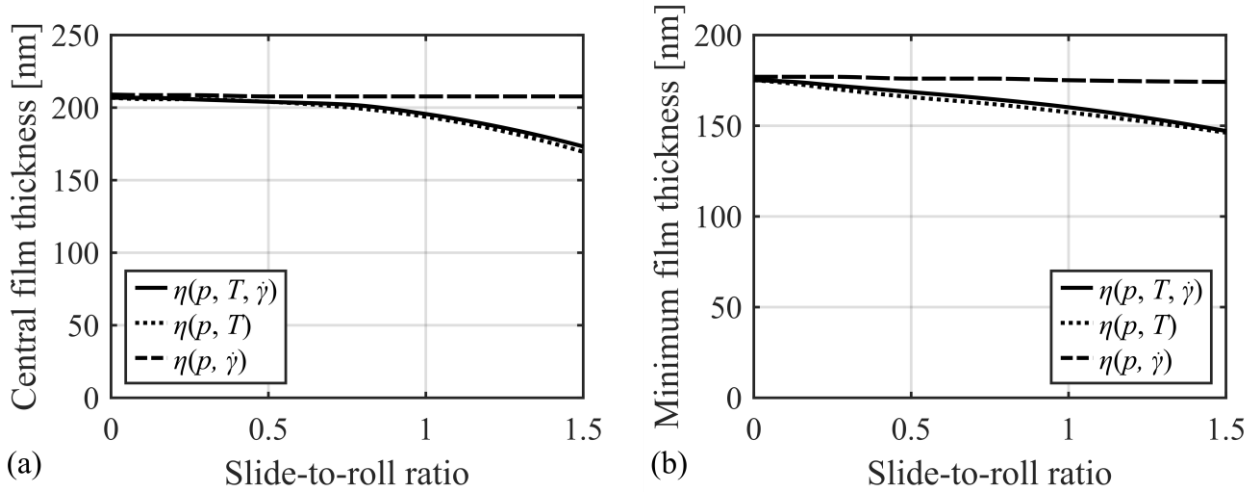



**Figure 5.** Variation in (**a**) central and (**b**) minimum film thickness as a function of the slide-to-roll ratio at a constant entrainment velocity of 2.5 $\text{m s}^{-1}$ predicted by the thermal shear-thinning (non-Newtonian) formulation $[\eta(p,T,\dot{\gamma})]$, the thermal Newtonian formulation $[\eta(p,T)]$ and the thermally uncoupled shear-thinning (isothermal non-Newtonian) formulation $[\eta(p,\dot{\gamma})]$.

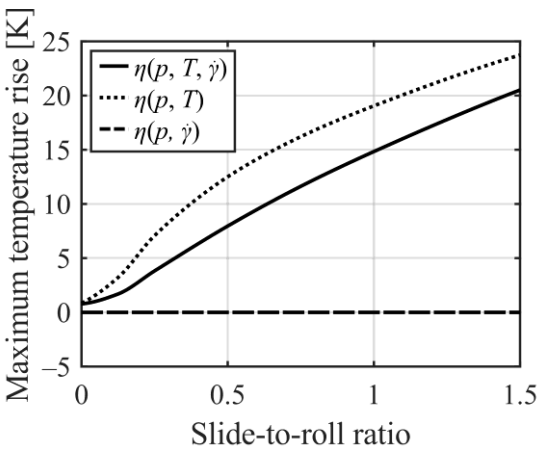



**Figure 6.** Variation in the maximum lubricant temperature rise $(\Delta T)$ as a function of the slide-to-roll ratio at a constant entrainment velocity of 2.5 $\text{m s}^{-1}$ predicted by the thermal shear-thinning

(non-Newtonian) formulation $[\eta(p,T,\dot{\gamma})]$, the thermal Newtonian formulation $[\eta(p,T)]$ and the thermally uncoupled shear-thinning (isothermal non-Newtonian) formulation $[\eta(p,\dot{\gamma})]$.

Figures 7–9 compare the cross-film temperature, viscosity and normalized velocity profiles at the centre of the contact (maximum contact pressure location) for two SRR values. These two SRR values were selected based on Figure 4b, where SRR = 0.25 is within the shear-thinning-dominated COF region and SRR = 1.5 corresponds to the thermal-softening-dominated COF region.

Figure 7 compares the temperature profiles across the lubricant film thickness at the centre of the contact (maximum contact pressure location), where $y^* = 1$ corresponds to the slower cylinder surface and $y^* = 0$ to the faster flat surface. At SRR = 0.25 [Figure 7a], both thermal formulations $[\eta(p,T,\dot{\gamma})\ and\ \eta(p,T)]$ showed symmetric profiles across the film thickness, with equal temperatures at the two walls and a maximum at the centre of the lubricant film. For the thermal Newtonian formulation $[\eta(p,T)]$, the temperature increased from 357 K at both walls to a maximum of 360 K at the film centre. For the thermal shear-thinning (non-Newtonian) formulation $[\eta(p,T,\dot{\gamma})]$, the entire temperature profile shifted to lower temperatures, with the maximum decreasing to 356.6 K, corresponding to a reduction of about 3.4 K. By contrast, the thermally uncoupled shear-thinning (isothermal non-Newtonian) formulation $[\eta(p,\dot{\gamma})]$ was maintained at the reference temperature $T_0 = 353$ K and therefore remained uniform across the film thickness.

At SRR = 1.5 [Figure 7b], the temperature distribution became markedly asymmetric as viscous dissipation increases. For the thermal Newtonian formulation $[\eta(p,T)]$, the temperature increased from approximately 364 K at the lower flat surface to a peak of 376.5 K near $y/h \approx 0.7$, before decreasing to 373.5 K at the upper cylinder surface. For the thermal shear-thinning (non-Newtonian) formulation $[\eta(p,T,\dot{\gamma})]$, the entire temperature profile was reduced, decreasing the peak temperature to 373 K and the lower flat surface temperature to 362 K. The lower temperatures predicted by this model indicate reduced viscous heat generation due to the lower effective viscosity produced by shear thinning.

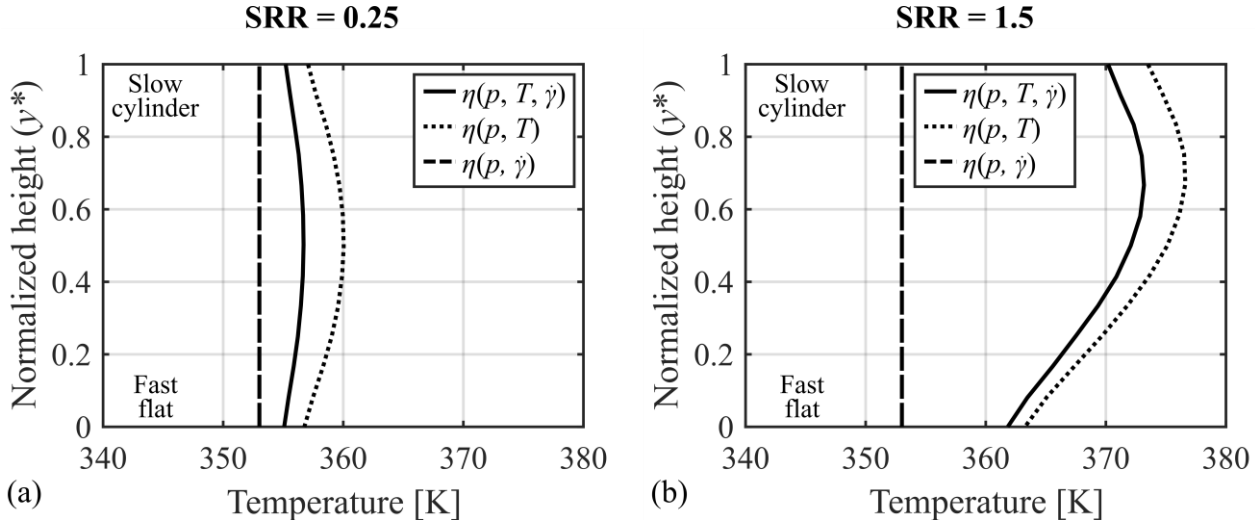



**Figure 7.** Cross-film temperature profiles at the centre of the contact (maximum contact pressure location) for the thermal shear-thinning (non-Newtonian) formulation $[\eta(p,T,\dot{\gamma})]$, the thermal Newtonian formulation $[\eta(p,T)]$ and the thermally uncoupled shear-thinning (isothermal non-Newtonian) formulation $[\eta(p,\dot{\gamma})]$ at (**a**) SRR = 0.25 and (**b**) SRR = 1.5, with a constant entrainment velocity of 2.5 m s$^{-1}$. Note: $y^* = 1$ corresponds to a slower cylinder surface, while $y^* = 0$ corresponds to a faster flat surface.

Figure 8 compares the viscosity profiles across the lubricant film thickness at the centre of the contact (maximum contact pressure location). At SRR = 0.25 [Figure 8a], the viscosity of the thermal shear-thinning (non-Newtonian) formulation $[\eta(p,T,\dot{\gamma})]$ decreased from 5.8 Pa · s at the lower flat surface to a minimum of 4.5 Pa · s at the film centre, before increasing to 5.7 Pa · s at the upper cylinder surface. For the thermal Newtonian formulation $[\eta(p,T)]$, the viscosity decreased from 13.7 Pa·s at the lower surface to approximately 7.7 Pa·s near the film centre, before increasing to 13.0 Pa·s at the upper surface. The thermally uncoupled shear-thinning (isothermal non-Newtonian) formulation $[\eta(p,\dot{\gamma})]$ remained nearly constant across the film at 6 Pa · s. All three viscosity profiles showed symmetric behaviour across the film thickness.

At SRR = 1.5 [Figure 8b], the viscosity distribution became strongly asymmetric. For the thermal Newtonian formulation $[\eta(p,T)]$, the viscosity decreased from 3.3 Pa · s at the lower flat surface to a minimum of 0.3 Pa · s at $y^* \approx 0.65$, followed by a slight increase to 0.50 Pa · s at the upper cylinder surface. For the thermal shear-thinning (non-Newtonian) formulation $[\eta(p,T,\dot{\gamma})]$, the viscosity at the lower flat surface was reduced to 2.2 Pa · s, while the minimum remains close to 0.3 Pa · s, followed by a slight increase to 0.49 Pa · s at the upper cylinder surface. The overlap of the thermal shear-thinning (non-Newtonian) $[\eta(p,T,\dot{\gamma})]$ and the thermal Newtonian $[\eta(p,T)]$ profiles over the upper part of the film suggests that thermal softening is the dominant viscosity reduction mechanism in this region. The thermally uncoupled shear-thinning (isothermal non-Newtonian) formulation $[\eta(p,\dot{\gamma})]$ remained nearly constant across the film at 1.5 Pa · s. The observed viscosities for the three analysed formulations show higher values at SRR = 0.25 [Figure 8a] than at SRR = 1.5 [Figure 8b], confirming the influence of shear thinning in both non-Newtonian formulations $[\eta(p,\dot{\gamma})$ and $\eta(p,T,\dot{\gamma})]$ and the effect of thermal softening in temperature-dependent viscosity formulations $[\eta(p,T)$ and $\eta(p,T,\dot{\gamma})]$.

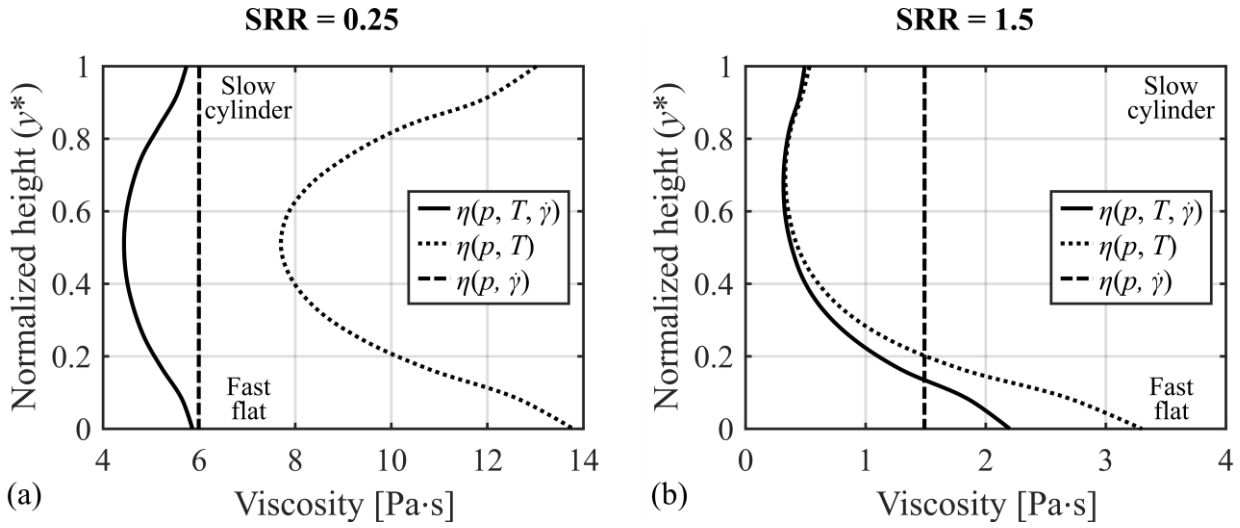



**Figure 8.** Cross-film viscosity profiles at the centre of the contact (maximum contact pressure location) for the thermal shear-thinning (non-Newtonian) formulation $[\eta(p,T,\dot{\gamma})]$, the thermal Newtonian formulation $[\eta(p,T)]$ and the thermally uncoupled shear-thinning (isothermal non-Newtonian) formulation $[\eta(p,\dot{\gamma})]$ at (**a**) SRR = 0.25 and (**b**) SRR = 1.5, with a constant entrainment velocity of 2.5 m s$^{-1}$. Note: $y^* = 1$ corresponds to a slower cylinder surface, while $y^* = 0$ corresponds to a faster flat surface, and the x-axis scale differs between Figure 8a,b.

Figure 9 presents the normalized cross-film velocity profiles. At SRR = 0.25 [Figure 9a], all three velocity profiles remained close to each other. Only slight differences were visible across the film.

At SRR = 1.5 [Figure 9b], larger differences were observed. The velocity profile for the thermally uncoupled shear-thinning (isothermal non-Newtonian) formulation $[\eta(p,\dot{\gamma})]$ follows the Couette flow profile. The velocity profiles for both thermal formulations (Newtonian and non-Newtonian) $[\eta(p,T,\dot{\gamma})$ and $\eta(p,T)]$ show stronger curvature, indicating that the velocity gradient is redistributed across the film thickness, with a larger velocity gradient toward the slower cylinder surface, where the temperature is higher and the effective viscosity is lower. Consequently, a larger fraction of the fluid across the film thickness moves at velocities closer to that of the faster flat surface.

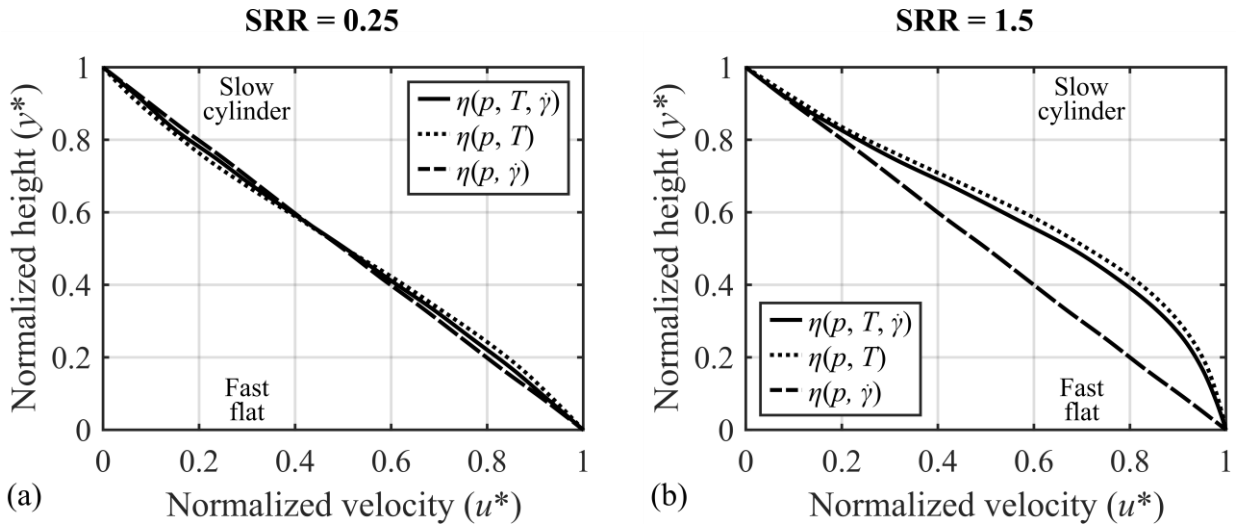



**Figure 9.** Normalized cross-film velocity profiles at the centre of the contact (maximum contact pressure location) for the thermal shear-thinning (non-Newtonian) formulation $[\eta(p,T,\dot{\gamma})]$, the thermal Newtonian formulation $[\eta(p,T)]$ and the thermally uncoupled shear-thinning (isothermal non-Newtonian) formulation $[\eta(p,\dot{\gamma})]$ at (**a**) SRR = 0.25 and (**b**) SRR = 1.5, with a constant entrainment velocity of 2.5 m s$^{-1}$. Note: $y^* = 1$ corresponds to a slower cylinder surface, while $y^* = 0$ corresponds to a faster flat surface.

### *3.2. Entrainment Velocity Variation*

The second set of simulations was performed at a fixed SRR of 1.5, while the entrainment velocity was varied from 0.5 to 2.5 m s$^{-1}$. Figure 10a shows the coefficient of friction as a function of entrainment velocity. For the thermal shear-thinning (non-Newtonian) formulation $[\eta(p,T,\dot{\gamma})]$, the coefficient of friction decreased from 0.030 at $u_e = 0.5$ m s$^{-1}$ to 0.019 at $u_e = 2.5$ m s$^{-1}$. For the thermal Newtonian formulation $[\eta(p,T)]$, it decreased from 0.050 to 0.022. For the thermally uncoupled shear-thinning (isothermal non-Newtonian) formulation $[\eta(p,\dot{\gamma})]$, it increased slightly from 0.038 to 0.042. At a fixed SRR, increasing the entrainment velocity also increases the sliding velocity and therefore the shear rate. The Eyring formulation reduces the rate at which shear stress increases with shear rate, but it does not impose a limiting shear stress. Consequently, shear stress, and therefore the COF, can still increase slightly with entrainment velocity.

Figure 10b shows the deviations in the COF with respect to the thermal shear-thinning (non-Newtonian) formulation $[\eta(p,T,\dot{\gamma})]$. The COF deviation associated with shear thinning decreased from 69.5% at $u_e = 0.5$ m s$^{-1}$ to 14.8% at $u_e = 2.5$ m s$^{-1}$. The COF deviation associated with thermal softening increased from 27.1% to 119.6%. These two curves crossed at $u_e \approx 0.87$ m s$^{-1}$, marking the transition from a shear-thinning-dominated COF to a thermal-softening-dominated COF.

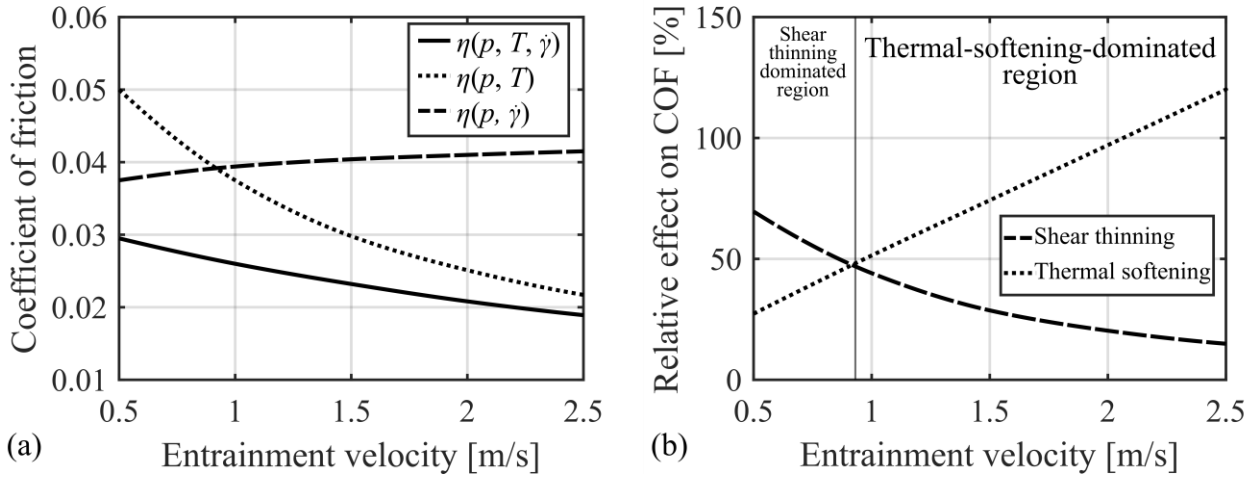



**Figure 10.** (**a**) Variation in the coefficient of friction and (**b**) deviations in the COF associated with shear thinning and thermal softening, evaluated with respect to the thermal shear-thinning (non-Newtonian) formulation $[\eta(p,T,\dot{\gamma})]$, as a function of entrainment velocity at a constant SRR of 1.5.

Figure 11a shows the variation in the central film thickness as a function of entrainment velocity. For the thermal shear-thinning (non-Newtonian) formulation $[\eta(p,T,\dot{\gamma})]$, the central film thickness increased from 65 nm at $u_e = 0.5\ \mathrm{m\,s^{-1}}$ to 173 nm at $u_e = 2.5\ \mathrm{m\,s^{-1}}$. For the thermal Newtonian formulation $[\eta(p,T)]$, it increased from 63 to 170 nm. For the thermally uncoupled shear-thinning (isothermal non-Newtonian) formulation $[\eta(p,\dot{\gamma})]$, it increased from 68 to 208 nm.

Figure 11b shows the variation in the minimum film thickness as a function of entrainment velocity. For the thermal shear-thinning (non-Newtonian) formulation $[\eta(p,T,\dot{\gamma})]$, the minimum film thickness increased from 55 to 147 nm. For the thermal Newtonian formulation $[\eta(p,T)]$, it increased from 52 to 146 nm. For the thermally uncoupled shear-thinning (isothermal non-Newtonian) formulation $[\eta(p,\dot{\gamma})]$, it increased from 58 to 174 nm. The difference between the thermal formulations $[\eta(p,T,\dot{\gamma})$ and $\eta(p,T)]$ and the isothermal formulation $[\eta(p,\dot{\gamma})]$ increased with entrainment velocity. The close agreement between the two thermal formulations, together with their increasing divergence from the isothermal formulation, indicates that under the investigated conditions, thermal softening is the dominant mechanism responsible for the film thickness differences at high entrainment velocity.

Figure 12 shows the maximum lubricant temperature rise $(\Delta T)$ as a function of entrainment velocity. For the thermal shear-thinning (non-Newtonian) formulation $[\eta(p,T,\dot{\gamma})]$, the maximum temperature rise increased from 7.20 K at $u_e = 0.5\ \mathrm{m\,s^{-1}}$ to 20.51 K at $u_e = 2.5\ \mathrm{m\,s^{-1}}$. For the thermal Newtonian formulation $[\eta(p,T)]$, it increased from 12.60 to 23.74 K. This formulation gave a higher maximum temperature rise than the thermal shear-thinning (non-Newtonian) formulation over all investigated entrainment velocities. The difference between the two formulations decreased as the entrainment velocity increased. For the thermally uncoupled shear-thinning (isothermal non-Newtonian) formulation, the temperature was prescribed as constant, and no temperature rise took place.

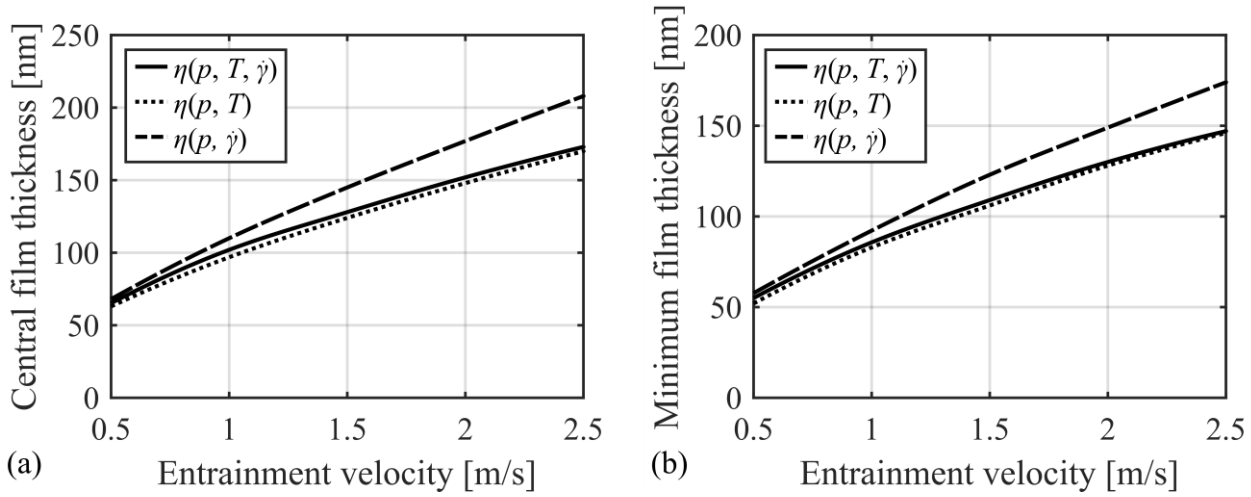



**Figure 11.** Variation in (**a**) central and (**b**) minimum film thickness as a function of entrainment velocity at a constant SRR of 1.5, predicted by the thermal shear-thinning (non-Newtonian) formulation $[\eta(p,T,\dot{\gamma})]$, the thermal Newtonian formulation $[\eta(p,T)]$ and the thermally uncoupled shear-thinning (isothermal non-Newtonian) formulation $[\eta(p,\dot{\gamma})]$.

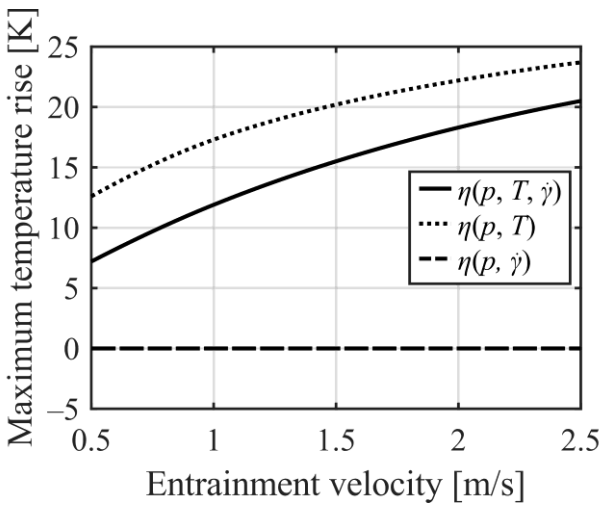



**Figure 12.** Variation in the maximum lubricant temperature rise $(\Delta T)$ as a function of entrainment velocity at a constant SRR of 1.5 predicted by the thermal shear-thinning (non-Newtonian) formulation $[\eta(p,T,\dot{\gamma})]$, the thermal Newtonian formulation $[\eta(p,T)]$ and the thermally uncoupled shear-thinning (isothermal non-Newtonian) formulation $[\eta(p,\dot{\gamma})]$.

The increase in maximum temperature with entrainment velocity describes the magnitude of the thermal response but not its streamwise development. To provide this spatial context, Figure 13 shows the temperature variation along the flat and cylinder interfaces for representative low- and high-entrainment-velocity conditions.

At $u_e = 0.5\ \mathrm{m\ s^{-1}}$, the temperatures of both surfaces increase gradually through the contact and remain close to each other. At $u_e = 2\ \mathrm{m\ s^{-1}}$, the temperature rise is substantially greater, and a larger temperature difference develops between the cylinder and flat surfaces, with the slower cylinder reaching the higher temperature. The streamwise distributions therefore show that increasing entrainment velocity at a fixed non-zero SRR increases the fluid temperature and enlarges the temperature difference between the contacting surfaces.

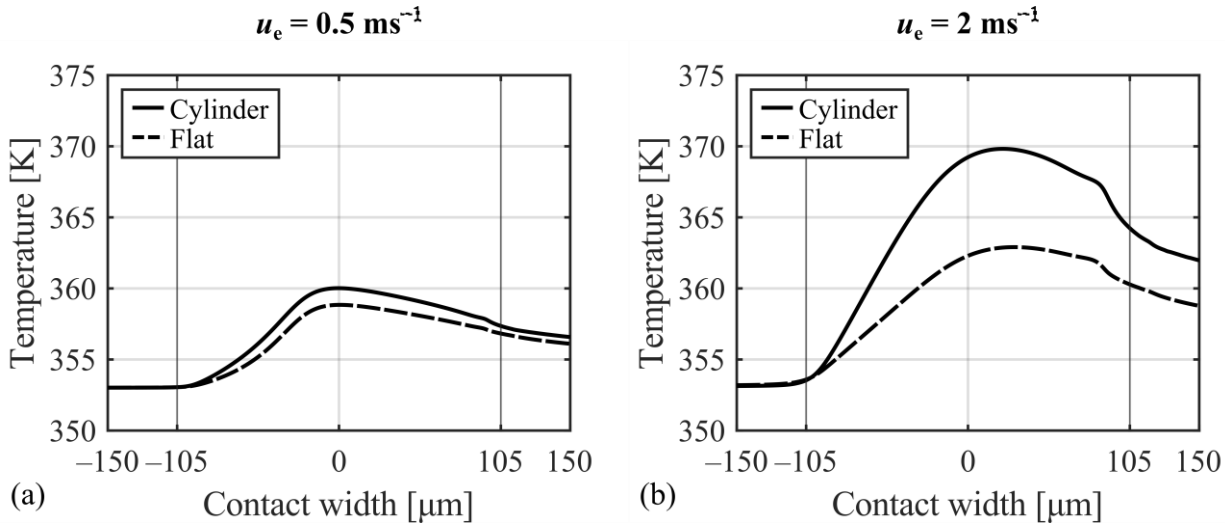



**Figure 13.** Fluid temperature variation along the contact at the cylinder and flat lubricant–solid interfaces for the thermal shear-thinning (non-Newtonian) formulation $[\eta(p,T,\dot{\gamma})]$ at (**a**) $u_e$ = 0.5 m s$^{-1}$ and (**b**) $u_e$ = 2 m s$^{-1}$, with a constant SRR of 1.5.

Figures 14–16 compare the normalized cross-film temperature, viscosity, and velocity profiles at the centre of the contact (maximum contact pressure location) for two entrainment velocities. These two entrainment velocities were selected based on Figure 10b, where $u_e$ = 0.5 m s$^{-1}$ is within the shear-thinning-dominated COF region and $u_e$ = 2 m s$^{-1}$ corresponds to the thermal-softening-dominated COF region.

Figure 14 compares the temperature profiles across the lubricant film thickness at the centre of the contact (maximum contact pressure location), where $y^* = 1$ corresponds to the slower cylinder surface and $y^* = 0$ to the faster flat surface. Because the SRR was fixed at 1.5, shear and heat generation were present at both entrainment velocities. The slower surface was hotter, while the faster surface was cooler. The temperature difference between the slower and faster surfaces was more pronounced at the higher entrainment velocity [compare Figure 14a,b] for both thermal formulations $[\eta(p,T,\dot{\gamma})$ and $\eta(p,T)]$. On the other hand, the thermally uncoupled shear-thinning (isothermal non-Newtonian) formulation $[\eta(p,\dot{\gamma})]$ was maintained at the reference temperature and remained uniform across the film thickness.

Figure 15 compares the viscosity profiles across the lubricant film thickness at the centre of the contact (maximum contact pressure location). Unlike the symmetric profiles at SRR = 0.25 in Figure 8a, the profiles at SRR = 1.5 and lower entrainment velocity in Figure 15a are asymmetric.

In both the shear-thinning-dominated COF region [Figure 15a] and the thermal-softening-dominated COF region [Figure 15b], the thermal shear-thinning (non-Newtonian) formulation $[\eta(p,T,\dot{\gamma})]$ and the thermal Newtonian formulation $[\eta(p,T)]$ showed lower viscosity at the slower surface (the cylinder) and higher viscosity at the faster surface (the flat). Additionally, over most of the film thickness, both thermal formulations $[\eta(p,T,\dot{\gamma})$ and $\eta(p,T)]$ predicted lower viscosities than the thermally uncoupled shear-thinning (isothermal non-Newtonian) formulation $[\eta(p,\dot{\gamma})]$. The latter formulation gave an almost constant viscosity across the film for both entrainment velocities.

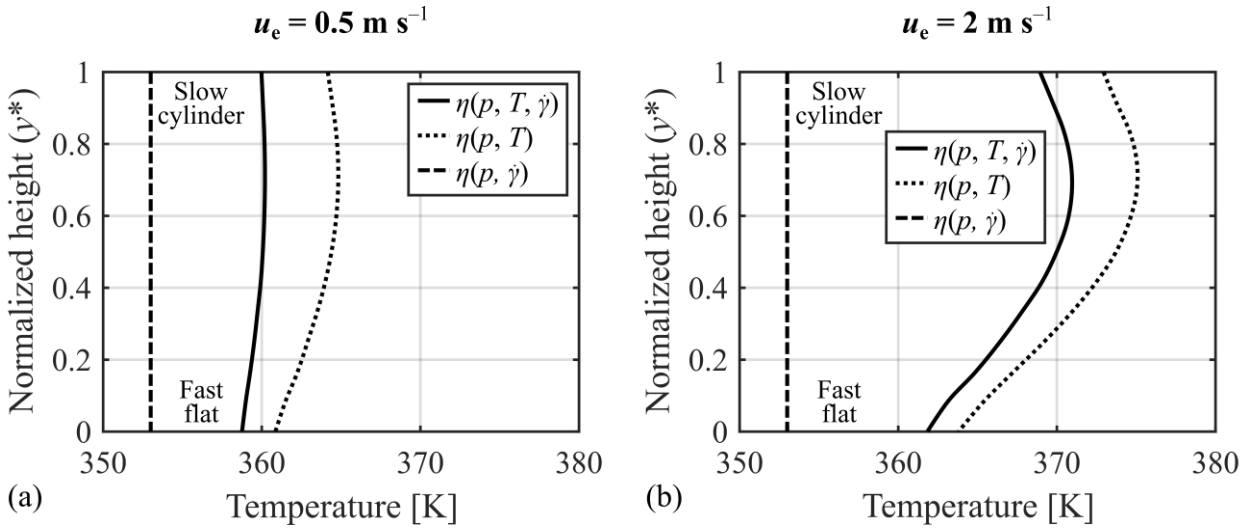



**Figure 14.** Cross-film temperature profiles at the centre of the contact (maximum contact pressure location) for the thermal shear-thinning (non-Newtonian) formulation $[\eta(p,T,\dot{\gamma})]$, the thermal Newtonian formulation $[\eta(p,T)]$ and the thermally uncoupled shear-thinning (isothermal non-Newtonian) formulation $[\eta(p,\dot{\gamma})]$ at (**a**) $u_e = 0.5$ m s$^{-1}$ and (**b**) $u_e = 2$ m s$^{-1}$, with a constant SRR of 1.5. Note: $y^* = 1$ corresponds to a slower cylinder surface, while $y^* = 0$ corresponds to a faster flat surface.

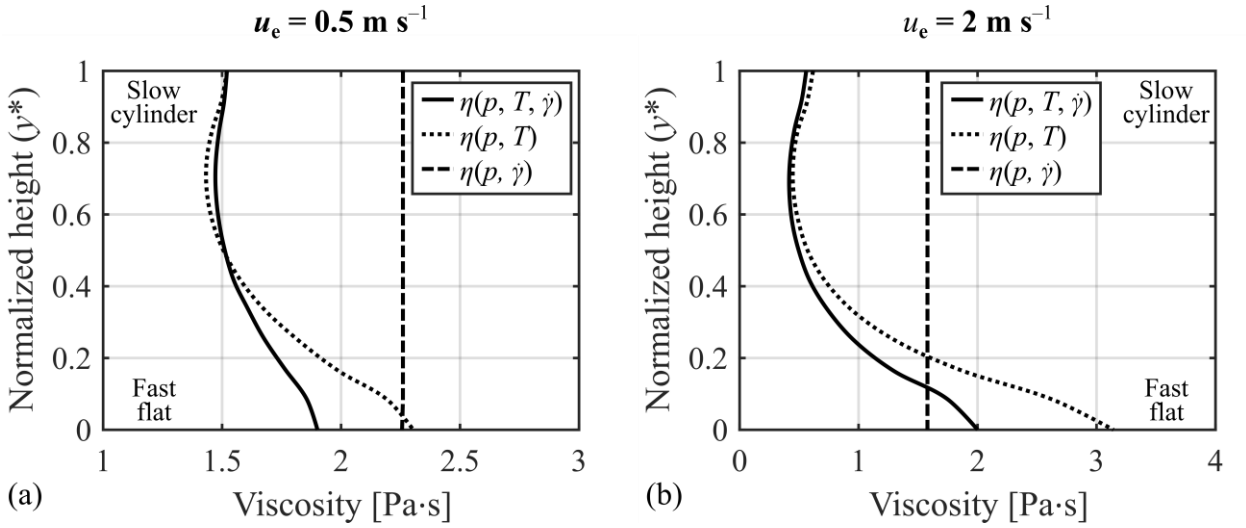



**Figure 15.** Cross-film viscosity profiles at the centre of the contact (maximum contact pressure location) for the thermal shear-thinning (non-Newtonian) formulation $[\eta(p,T,\dot{\gamma})]$, the thermal Newtonian formulation $[\eta(p,T)]$ and the thermally uncoupled shear-thinning (isothermal non-Newtonian) formulation $[\eta(p,\dot{\gamma})]$ at (**a**) $u_e = 0.5$ m s$^{-1}$ and (**b**) $u_e = 2$ m s$^{-1}$, with a constant SRR of 1.5. Note: $y^* = 1$ corresponds to a slower cylinder surface, while $y^* = 0$ corresponds to a faster flat surface, and the x-axis scale differs between panels (**a**,**b**).

Figure 16 presents the normalized cross-film velocity profiles. In the shear-thinning-dominated COF region [Figure 16a], all three profiles remained close to each other. Only slight differences were visible over the film thickness. In contrast, in the thermal-softening-dominated COF region [Figure 16b], stronger curvature was observed for both thermal formulations.

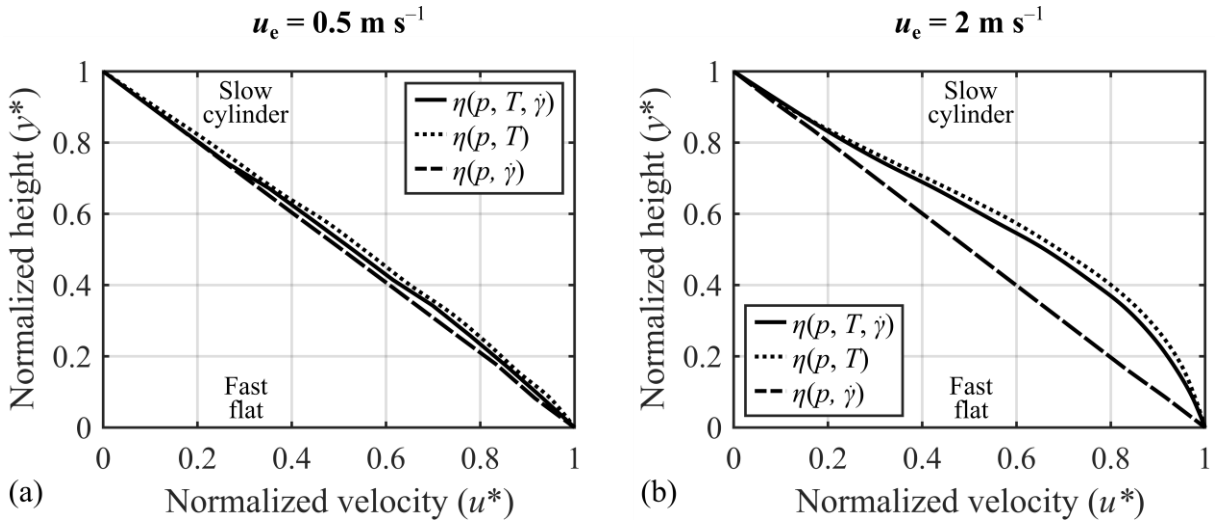



**Figure 16.** Normalized cross-film velocity profiles at the centre of the contact (maximum contact pressure location) for the thermal shear-thinning (non-Newtonian) formulation $[\eta(p,T,\dot{\gamma})]$, the thermal Newtonian formulation $[\eta(p,T)]$ and the thermally uncoupled shear-thinning (isothermal non-Newtonian) formulation $[\eta(p,\dot{\gamma})]$ at (**a**) $u_e = 0.5$ m s$^{-1}$ and (**b**) $u_e = 2$ m s$^{-1}$, with a constant SRR of 1.5. Note: $y^* = 1$ corresponds to a slower cylinder surface, while $y^* = 0$ corresponds to a faster flat surface.

## 4. Discussion

### *4.1. Shear-Thinning Mechanism*

The three viscosity formulations provide a controlled comparison of thermal softening and shear thinning and their relative influences on friction and film thickness. The thermal Newtonian formulation $[\eta(p,T)]$ excludes shear thinning from the fully coupled thermal shear-thinning (non-Newtonian) formulation $[\eta(p,T,\dot{\gamma})]$, whereas the isothermal non-Newtonian formulation $[\eta(p,\dot{\gamma})]$ excludes thermal softening. The difference between each reduced formulation and the fully coupled thermal non-Newtonian formulation $[\eta(p,T,\dot{\gamma})]$ therefore quantifies the effect of excluding the corresponding viscosity dependence. These differences are not additive because shear thinning also influences viscous heat generation and, consequently, the thermal response [9,25,70].

Increasing the SRR at a fixed entrainment velocity, or increasing entrainment velocity at a fixed non-zero SRR, also increases the sliding speed and the resulting shear rate in the lubricant film. In the isothermal non-Newtonian formulation $[\eta(p,\dot{\gamma})]$, shear thinning reduces the effective viscosity, which remains approximately uniform across the film thickness at the contact centre (Figures 8 and 15). At a given pressure, temperature, and shear rate, shear thinning reduces shear stress relative to Newtonian behaviour and contributes to the lower COF predicted by the thermal non-Newtonian formulation $[\eta(p,T,\dot{\gamma})]$ compared with the thermal Newtonian formulation $[\eta(p,T)]$ [Figures 4a and 10a]. Near the maximum pressure location, the streamwise pressure gradient is small, resulting in an approximately uniform shear stress across the film. Consequently, the local shear rates and velocity gradients remain nearly uniform, and the velocity profile approaches linear Couette flow (Figures 9 and 16). The cross-film average lubricant velocity therefore remains approximately equal to the entrainment velocity (Figure 17), consistent with the nearly constant film thickness predicted by the isothermal formulation as the SRR increases (Figure 5).

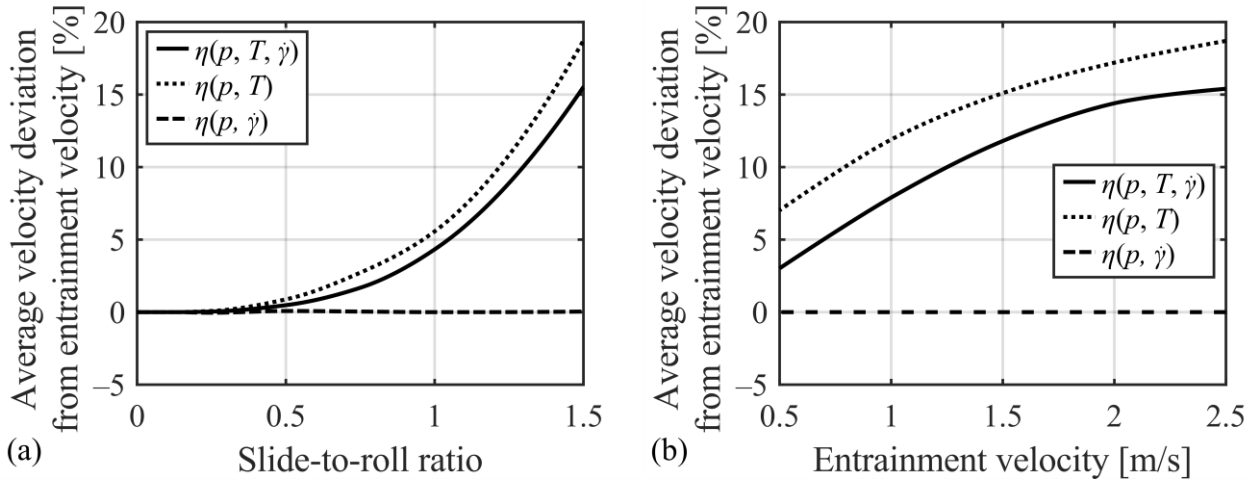



**Figure 17.** Average velocity deviation from the entrainment velocity at the contact centre as a function of (**a**) the slide-to-roll ratio (entrainment velocity = 2.5 $m{\cdot}s^{-1}$) and (**b**) entrainment velocity (SRR = 1.5) for the thermal shear-thinning (non-Newtonian) formulation $[\eta(p,T,\dot{\gamma})]$, the thermal Newtonian formulation $[\eta(p,T)]$ and the thermally uncoupled shear-thinning (isothermal non-Newtonian) formulation $[\eta(p,\dot{\gamma})]$.

### *4.2. Thermal Softening Mechanism*

In the thermal formulations [$\eta(p,T)$ and $\eta(p,T,\dot{\gamma})$], viscous heating raises the lubricant temperature (Figures 6 and 12), thereby lowering the local lubricant viscosity (Figures 8 and 15). This viscosity reduction contributes to lower wall shear stresses and consequently to the lower COF predicted by the thermal non-Newtonian formulation compared with the isothermal non-Newtonian formulation [Figures 4a and 10a]. At a high SRR, viscous heating and heat exchange with the contacting surfaces moving at different speeds produce an asymmetric cross-film temperature distribution [Figures 7b and 14]. The lubricant near the slower cylinder surface becomes hotter and exhibits lower viscosity (Figures 8b and 15), whereas the lubricant near the faster flat surface remains cooler and retains higher viscosity (Figures 8b and 15).

This non-uniform viscosity distribution modifies the local velocity gradient across the film thickness. Because the shear stress remains approximately constant across the film at the contact centre, a lower viscosity corresponds to a higher shear rate, whereas a higher viscosity corresponds to a lower shear rate [see Equation (28)]. Accordingly, the velocity gradient increases in the hotter, lower-viscosity region near the slower surface, while the velocity gradient decreases in the cooler, higher-viscosity region near the faster surface [Figures 9b and 16b]. This redistribution of the velocity gradient produces a nonlinear velocity profile, with a larger fraction of the lubricant moving at velocities closer to that of the faster surface [Figures 9b and 16b]. The resulting increase in cross-film average velocity is quantified in Figure 17.

$$\tau_{xy} \approx \eta \frac{\partial u}{\partial y} \tag{28}$$

Figure 17 shows the deviation of the cross-sectional average lubricant velocity from the entrainment velocity at the centre of the Hertzian contact. For the thermally uncoupled shear-thinning (isothermal non-Newtonian) formulation $[\eta(p,\dot{\gamma})]$, the velocity deviation remains approximately zero over the entire SRR range, consistent with an almost linear Couette velocity profile (Figures 9 and 16). In contrast, both thermal formulations [$\eta(p,T,\dot{\gamma})$ and $\eta(p,T)$] show an increase in the average lubricant velocity with an increasing SRR. As an example, at SRR $= 1.5$, the mean velocity exceeds the entrainment velocity ($u_e$) by approximately 15.6% for the thermal shear-thinning (non-Newtonian)

formulation $[\eta(p,T,\dot{\gamma})]$ and 18.8% for the thermal Newtonian formulation $[\eta(p,T)]$. Consistent with mass conservation, the increase in cross-film average velocity is thus associated with lower film thickness in both thermal formulations, as shown by the decrease in film thickness with an increasing SRR (Figure 5) and the increasingly lower thicknesses relative to the isothermal formulation as entrainment velocity increases at a fixed non-zero SRR (Figure 11).

This newly proposed mechanism for reduced film thickness due to nonlinear viscosity and velocity distributions across the film was also validated in EHL experiments. Figure 18 presents complementary film thickness measurements using PAO6 oil in an EHD apparatus (PCS Instruments Ltd., London, UIK) at an entrainment velocity of 2.2 m/s, a temperature of 298.15 K (25 °C) and a normal load of 20 N. Central and minimum film thicknesses decreased with increasing SRRs, with a larger reduction in minimum film thickness. This trend is qualitatively consistent with the film reduction with the SRR presented in Figure 5 for thermal formulations $[\eta(p,T,\dot{\gamma})$ and $\eta(p,T)]$.

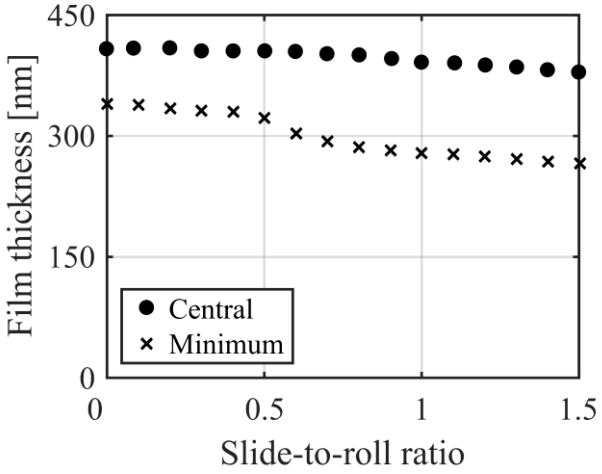



**Figure 18.** Central and minimum film thickness of PAO6 measured by optical interferometry using a PCS Instruments EHD apparatus, as a function of the SRR at an entrainment velocity of 2.2 m/s, a temperature of 298.15 K, and a normal load of 20 N.

A comparison of the two thermal formulations $[\eta(p,T)$ and $\eta(p,T,\dot{\gamma})]$ also reveals the interaction between shear thinning and thermal softening. The thermal Newtonian formulation $[\eta(p,T)]$ produces the highest maximum lubricant temperature rise (Figures 6 and 12) and the largest average velocity deviation from the entrainment velocity (Figure 17). In the thermal shear-thinning (non-Newtonian) formulation $[\eta(p,T,\dot{\gamma})]$, shear thinning lowers the shear stress and consequently reduces the viscous heat generation. Shear thinning therefore limits the temperature rise (Figures 6, 7, 12 and 14) and weakens the thermal softening (Figures 8 and 15) that would otherwise develop.

### *4.3. Effect of Different Shear-Thinning and Thermal Softening Models on Key Mechanisms*

To assess whether the identified mechanisms depend on the original constitutive equations, we conducted additional simulations using the modified Carreau–Yasuda model [57] to describe shear thinning and the Vogel-like thermodynamic scaling model [58] to describe low-shear viscosity with experimentally based rheological properties of Shell T9 mineral oil, reported by Habchi et al. [59]. Below, we present just the key results that describe the most essential findings and the novel film thickness reduction mechanism, and we compare those findings with those obtained using the Eyring [21] and Roelands [50] models that are used throughout this work.

Figure 19 presents the cross-film temperature and velocity distributions at SRR = 0.25 and 1.5. The inlet temperature was 298.15 K, and the entrainment velocity was 2.5 m/s. The thermal non-Newtonian formulation $[\eta(p,T,\dot{\gamma})]$ and the isothermal non-Newtonian formulation $[\eta(p,\dot{\gamma})]$ are compared at both SRRs, while the thermal Newtonian formulation $[\eta(p,T)]$ is also included at SRR = 1.5 to examine the influence of shear thinning under thermal conditions.

At SRR = 0.25, Figure 19a shows that the temperature predicted by the thermal non-Newtonian formulation $[\eta(p,T,\dot{\gamma})]$ increases slightly above the inlet temperature, with a maximum near the film centre. Figure 19c shows that the thermal non-Newtonian formulation $[\eta(p,T,\dot{\gamma})]$ and the isothermal non-Newtonian formulation $[\eta(p,\dot{\gamma})]$ produce similar, nearly linear velocity profiles. These results agree with Figures 7a and 9a in Section 3.1, where the limited temperature rise at a low SRR is accompanied by only small differences in the cross-film velocity profiles.

At SRR = 1.5, Figure 19b shows that the temperature distributions become asymmetric, with the maximum temperature located closer to the slower cylinder surface. The thermal Newtonian formulation $[\eta(p,T)]$ predicts a higher maximum temperature than the thermal non-Newtonian formulation $[\eta(p,T,\dot{\gamma})]$, approximately 375 K compared with 346 K. This difference shows that shear thinning limits the temperature increase. The same behaviour was observed in Figure 7b in Section 3.1 using the original rheological formulations.

Figure 19d shows that the isothermal non-Newtonian formulation $[\eta(p,\dot{\gamma})]$ maintains a nearly linear velocity profile, whereas both thermal formulations $[\eta(p,T,\dot{\gamma})$ and $\eta(p,T)]$ produce nonlinear profiles. The velocity gradient becomes greater near the slower cylinder surface, where the temperature is higher. Consequently, a larger portion of the lubricant moves at velocities closer to that of the faster flat surface. The thermal Newtonian formulation $[\eta(p,T)]$ exhibits a slightly greater deviation from the isothermal profile than the thermal non-Newtonian formulation $[\eta(p,T,\dot{\gamma})]$. These results agree with Figure 9b in Section 3.1, where thermal softening produces the same redistribution of the cross-film velocity profile.

These additional calculations reproduce the principal physical findings of this work by using different shear-thinning (modified Carreau–Yasuda) and thermal softening (Vogel-like thermodynamic scaling) models, as well as different lubricants, compared with those used throughout the comprehensive analyses in this study. This agreement in the qualitative mechanisms demonstrates that the findings presented are not restricted to the combined Roelands and Eyring formulations that are mainly used in this work. More comprehensive investigations into individual responses and sensitivity to various lubricant properties and contact conditions are already underway to quantify the influence of different rheological formulations and lubricant properties on friction and film thickness.

### *4.4. The Transition Between Shear Thinning and Thermal Softening*

At a low non-zero SRR, shear thinning has a greater influence on the COF, whereas at high SRRs, thermal softening dominates [Figure 4b]. Similarly, at a fixed slide-to-roll ratio, shear thinning has a greater influence on the COF at low entrainment velocity, whereas thermal softening has a larger influence on the COF at high entrainment velocity [Figure 10b]. Increasing either the SRR at a fixed entrainment velocity or entrainment velocity at a fixed non-zero SRR therefore increases the relative importance of thermal softening for the COF. Since sliding speed $\Delta u$ is given by $u_e \cdot \mathrm{SRR}$, increasing sliding speed favours the transition from shear-thinning-dominated to thermal-softening-dominated COF behaviour. The exact transition point is expected to depend on the lubricant and contact conditions, but sliding speed provides a useful parameter for interpreting the relative importance of the two mechanisms. This is schematically shown in Figure 20.

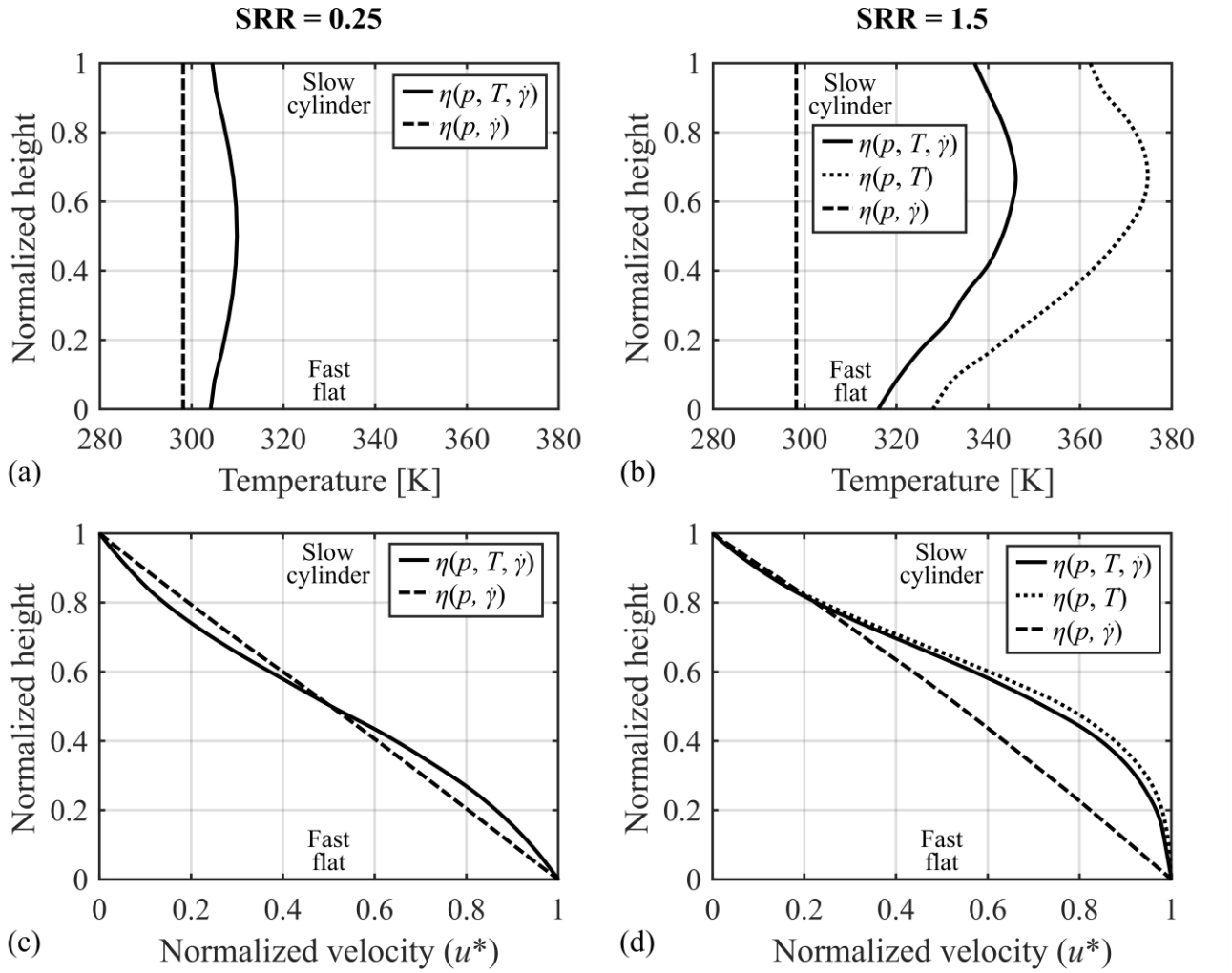



**Figure 19.** Cross-film distributions using the modified Carreau–Yasuda shear-thinning and Vogel-like thermodynamic scaling viscosity formulations, with rheological parameters for Shell T9: (**a**,**b**) temperature and (**c**,**d**) normalized streamwise velocity at SRR = 0.25 (**left column**) and SRR = 1.5 (**right column**). The entrainment velocity is 2.5 m/s, and the inlet temperature is 298.15 K. The profiles are evaluated at the contact centre.

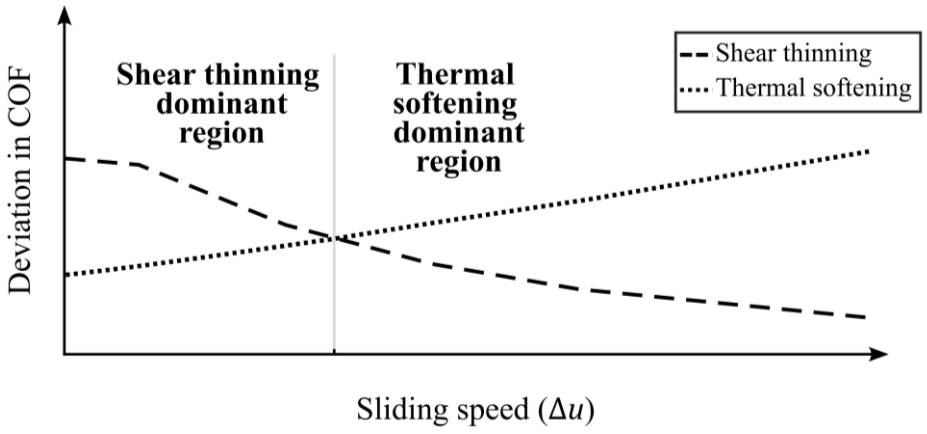



**Figure 20.** Qualitative schematic representation of the transition from shear-thinning-dominated to thermal-softening-dominated COF behaviour with increasing sliding speed.

https://doi.org/10.3390/lubricants14110417

## 5. Conclusions

The controlled comparisons reveal distinct friction and film thickness responses to shear rate and temperature dependence within the investigated EHL line-contact conditions. The main findings are:

1. Shear thinning mainly influences friction and has a much smaller effect on film thickness, which is evident from the comparison of the thermal shear-thinning (non-Newtonian) formulation $[\eta(p,T,\dot{\gamma})]$ and the thermal Newtonian $[\eta(p,T)]$ formulation. The film thickness predictions of these two formulations are close, whereas their COF values differ considerably, particularly at low SRRs and low entrainment velocity.
2. Thermal softening affects both friction and film thickness. This is evident from the comparison between the thermal formulations $[\eta(p,T,\dot{\gamma})$ and $\eta(p,T)]$ and the isothermal non-Newtonian $[\eta(p,\dot{\gamma})]$ formulation.
3. A novel mechanism for reduced film thickness due to nonlinear viscosity and velocity distributions across the film was found at high SRRs due to thermal effects. Both thermal formulations $[\eta(p,T,\dot{\gamma})$ and $\eta(p,T)]$ exhibit a non-uniform cross-film viscosity distribution at the contact centre, with lower viscosity near the hotter, slower surface and higher viscosity near the cooler, faster surface. This redistributes the velocity gradient, producing a nonlinear velocity profile and increasing the cross-film average lubricant velocity. The resulting velocity redistribution leads to a film thickness reduction.
4. Across the investigated ranges, the thermal formulations produced increasingly lower film thicknesses relative to the isothermal shear-thinning formulation as the SRR or entrainment velocity increased.
5. The relative influence of shear thinning and thermal softening on friction varies with sliding speed. At low sliding speed (low entrainment velocity and/or low SRR), shear thinning has the greater influence, whereas thermal softening becomes more important at high sliding speed (high entrainment velocity and/or high SRR).
6. The qualitative agreement observed in the limited additional analyses using alternative shear-thinning (Eyring and modified Carreau–Yasuda) and pressure–temperature viscosity (Roelands and Vogel-like) formulations demonstrates that the key physical mechanisms identified in this work are not restricted to the specific rheological formulations. More comprehensive analyses are needed to quantify the influence of different rheological formulations and lubricant properties on friction and film thickness.

**Author Contributions:** Conceptualization, R.A. and M.K.; methodology, R.A., M.P. and M.K.; software, R.A.; validation, R.A. and M.P.; formal analysis, R.A. and M.P.; investigation, R.A.; resources, M.K.; data curation, R.A. and M.P.; writing—original draft preparation, R.A.; writing—review and editing, M.P. and M.K.; visualization, R.A. and M.P.; supervision, M.K. and M.P.; project administration, M.K.; funding acquisition, M.K. All authors have read and agreed to the published version of the manuscript.

**Funding:** This research was funded by the Slovenian Research and Innovation Agency (ARIS) under core grant No. P2-0231.

**Data Availability Statement:** The data presented in this study are available on request from the corresponding author.

**Conflicts of Interest:** The authors declare no conflicts of interest.

## Abbreviations and Symbols

The following abbreviations and symbols are used in this manuscript:

| Symbol | Description | Unit |
|---|---|---|
| **Abbreviations** | | |
| COF | Coefficient of friction | |
| CFD | Computational fluid dynamics | |
| EHL | Elastohydrodynamic lubrication | |
| SRR | Slide-to-roll ratio | |
| **List of Symbols** | | |
| General variables: | | |
| $\Omega$ | Computational domain/integration region | – |
| $T$ | Temperature | [K] |
| $T_0$ | Reference temperature | [K] |
| $p$ | Pressure | [Pa] |
| $t$ | Time | [s] |
| Fluid properties and variables: | | |
| $\alpha_\mathrm{l}$ | Lubricant volume fraction | – |
| $\alpha_\mathrm{v}$ | Vapour volume fraction | – |
| $\alpha$ | Pressure–viscosity coefficient | [$Pa^{-1}$] |
| $\beta$ | Thermo-viscous constant | [$K^{-1}$] |
| $\beta_T$ | Volumetric coefficient of thermal expansion | [$K^{-1}$] |
| $\dot{\gamma}$ | Shear rate | [$s^{-1}$] |
| $\eta$ | Dynamic viscosity | [Pa·s] |
| $\eta_0$ | Ambient viscosity | [Pa·s] |
| $\rho_\mathrm{l}$ | Lubricant density | [kg·$m^{-3}$] |
| $\rho_\mathrm{m}$ | Mixture density | [kg·$m^{-3}$] |
| $\rho_\mathrm{v}$ | Vapour density | [kg·$m^{-3}$] |
| $\rho_0$ | Ambient density | [kg·$m^{-3}$] |
| $\boldsymbol{\sigma}_\mathrm{f}$ | Fluid stress tensor | [Pa] |
| $\tau_0$ | Eyring stress | [Pa] |
| $\tau_\mathrm{w}$ | Wall shear stress | [Pa] |
| $\tau_{xy}$ | Streamwise cross-film shear stress | [Pa] |
| $c_{p,\,\mathrm{m}}$ | Fluid heat capacity at constant pressure | [J·$kg^{-1}$·$K^{-1}$] |
| $k_\mathrm{m}$ | Mixture thermal conductivity | [W·$m^{-1}$·$K^{-1}$] |
| $\mathbf{u_m}$ | Mixture velocity vector | [m·$s^{-1}$] |
| Solid properties and variables: | | |
| $\boldsymbol{\varepsilon}$ | Strain tensor | – |
| $\nu$ | Poisson's ratio | – |
| $\rho_\mathrm{s}$ | Solid density | [kg·$m^{-3}$] |
| $\boldsymbol{\sigma}_\mathrm{s}$ | Solid stress tensor | [Pa] |
| $\mathbf{C}$ | Stiffness tensor | [Pa] |
| $E$ | Elastic modulus | [Pa] |
| $E_\mathrm{rc}$ | Cylinder reduced elastic modulus | [Pa] |
| $c_{p,\,\mathrm{s}}$ | Solid heat capacity at constant pressure | [J·$kg^{-1}$·$K^{-1}$] |
| $k_\mathrm{s}$ | Solid thermal conductivity | [W·$m^{-1}$·$K^{-1}$] |
| Geometric parameters: | | |
| $R$ | Radius | [m] |
| $R_\mathrm{rc}$ | Equivalent radius | [m] |
| $a$ | Hertzian contact half-width | [m] |
| $x$, $y$, and $z$ | Spatial coordinates | [m] |
| Operational parameters: | | |
| $u_\mathrm{c}$ | Cylinder's velocity | [m·$s^{-1}$] |
| $u_\mathrm{f}$ | Flat's velocity | [m·$s^{-1}$] |
| $u_\mathrm{e}$ | Entrainment velocity | [m·$s^{-1}$] |
| $W'$ | Normal load per unit length | [N·$m^{-1}$] |
| Thermal parameters: | | |
| $Q_\mathrm{comp}$ | Compressional heat generation | [W·$m^{-3}$] |

| | | |
|---|---|---|
| $Q_{\text{shear}}$ | Viscous shear heat generation | [W·m$^{-3}$] |
| $T_{\text{f}}$ | Fluid temperature | [K] |
| $T_{\text{s}}$ | Solid surface temperature | [K] |
| $\mathbf{n}$ | Outward unit normal from the fluid domain | [–] |
| $\hat{q}_f$ | Interfacial heat flux from fluid to solid | [W·m$^{-2}$] |
| $s$ | Surface coordinate in Carslaw–Jaeger formulation | [m] |
| $\hat{s}$ | Source coordinate in Carslaw–Jaeger formulation | [m] |
| $u_{\text{s}}$ | Local surface speed in the Carslaw–Jaeger formulation | [m·s$^{-1}$] |
| Mathematical operators: | | |
| $\cdot$ | Dot operator | – |
| $\otimes$ | Tensor (Outer) product | – |
| $\nabla$ | Gradient operator | [m$^{-1}$] |

## Appendix A

*Appendix A.1*

The isothermal EHL line-contact model was validated by comparing the predicted pressure and film thickness distributions with the reference results reported by Singh et al. [71] and those obtained using Habchi's solver [64]. Singh et al. [71] employed a Navier–Stokes formulation, whereas Habchi's solver [64] was based on the Reynolds equation. The comparison in Figure A1 therefore assesses the present solution against two independent numerical formulations.

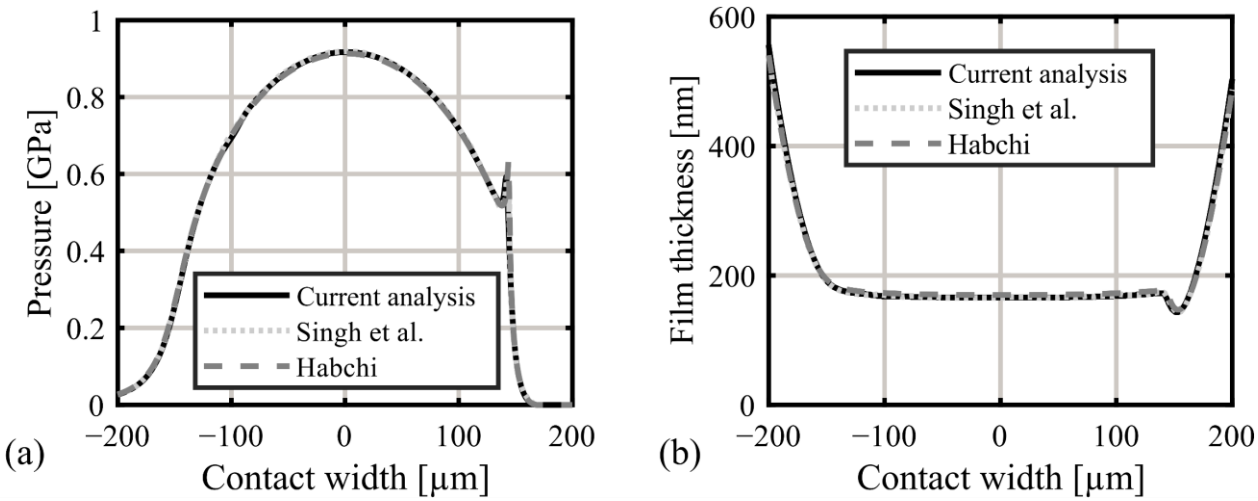



**Figure A1.** Model validation against Singh et al. [71] and Habchi [64]: (**a**) Pressure and (**b**) film thickness distributions across the contact for $u_{\text{e}} = 0.575$ m s$^{-1}$, $W' = 231$ kN m$^{-1}$, and $\eta_0 = 0.04$ Pa·s.

*Appendix A.2*

The thermal EHL line-contact model was validated against the reference results reported by Hartinger et al. [70]. The validation calculations used the same geometry, lubricant properties and operating conditions as the reference study. Figure A2 compares the predicted pressure and film thickness distributions with the results of Hartinger et al. [70].

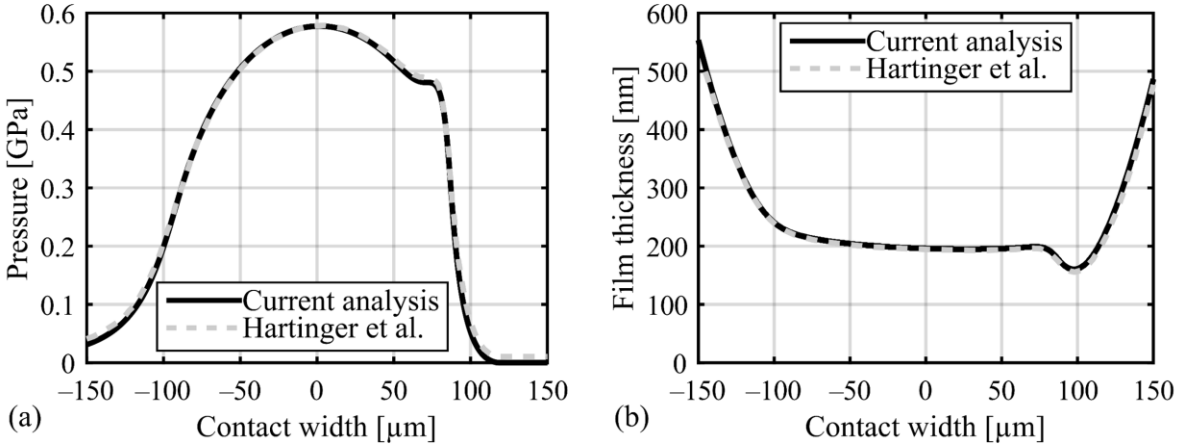



**Figure A2.** Model validation against Hartinger et al. [70]: (**a**) pressure distribution and (**b**) film thickness distributions across the contact for $u_e = 2.5$ m s$^{-1}$, $W' = 100$ kN m$^{-1}$, $\eta_0 = 0.01$ Pa·s, SRR = +1, and $T_0 = 353$ K.

## References


1. Spikes, H.A. Sixty years of EHL. *Lubr. Sci.* **2006**, *18*, 265–291. https://doi.org/10.1002/ls.23.
2. Lugt, P.M.; Morales-Espejel, G.E. A Review of Elasto-Hydrodynamic Lubrication Theory. *Tribol. Trans.* **2011**, *54*, 470–496. https://doi.org/10.1080/10402004.2010.551804.
3. Gohar, R. *Elastohydrodynamics*, 2nd ed.; Imperial College Press: London, UK, 2001.
4. Dowson, D. Elastohydrodynamic and micro-elastohydrodynamic lubrication. *Wear* **1995**, *190*, 125–138. https://doi.org/10.1016/0043-1648(95)06660-8.
5. Greenwood, J.A. Elastohydrodynamic Lubrication. *Lubricants* **2020**, *8*, 51. https://doi.org/10.3390/lubricants8050051.
6. Tošić, M.; Larsson, R.; Jovanović, J.; Lohner, T.; Björling, M.; Stahl, K. A Computational Fluid Dynamics Study on Shearing Mechanisms in Thermal Elastohydrodynamic Line Contacts. *Lubricants* **2019**, *7*, 69. https://doi.org/10.3390/lubricants7080069.
7. Spikes, H.; Zhang, J. History, Origins and Prediction of Elastohydrodynamic Friction. *Tribol. Lett.* **2014**, *56*, 1–25. https://doi.org/10.1007/s11249-014-0396-y.
8. Liu, Y.; Wang, Q.J.; Bair, S.; Vergne, P. A Quantitative Solution for the Full Shear-Thinning EHL Point Contact Problem Including Traction. *Tribol. Lett.* **2007**, *28*, 171–181. https://doi.org/10.1007/s11249-007-9262-5.
9. Kumar, P.; Khonsari, M.M. Combined Effects of Shear Thinning and Viscous Heating on EHL Characteristics of Rolling/Sliding Line Contacts. *J. Tribol.* **2008**, *130*, 041505. https://doi.org/10.1115/1.2959111.
10. Habchi, W.; Bair, S.; Vergne, P. On friction regimes in quantitative elastohydrodynamics. *Tribol. Int.* **2013**, *58*, 107–117. https://doi.org/10.1016/j.triboint.2012.10.005.
11. MacLaren, A.; Kadiric, A. Elastohydrodynamic Traction and Film Thickness at High Speeds. *Tribol. Lett.* **2024**, *72*, 92. https://doi.org/10.1007/s11249-024-01894-w.
12. Houpert, L. New Results of Traction Force Calculations in Elastohydrodynamic Contacts. *J. Tribol.* **1985**, *107*, 241–245. https://doi.org/10.1115/1.3261033.
13. Houpert, L.G.; Hamrock, B.J. Fast Approach for Calculating Film Thicknesses and Pressures in Elastohydrodynamically Lubricated Contacts at High Loads. *J. Tribol.* **1986**, *108*, 411–419. https://doi.org/10.1115/1.3261220.
14. Cheng, H.S.; Sternlicht, B. A Numerical Solution for the Pressure, Temperature, and Film Thickness Between Two Infinitely Long, Lubricated Rolling and Sliding Cylinders, Under Heavy Loads. *J. Basic. Eng.* **1965**, *87*, 695–704. https://doi.org/10.1115/1.3650647.
15. Cheng, H.S. A Refined Solution to the Thermal-Elastohydrodynamic Lubrication of Rolling and Sliding Cylinders. *ASLE Trans.* **1965**, *8*, 397–410. https://doi.org/10.1080/05698196508972110.
16. Wolff, R.; Nonaka, T.; Kubo, A.; Matsuo, K. Thermal Elastohydrodynamic Lubrication of Rolling/Sliding Line Contacts. *J. Tribol.* **1992**, *114*, 706–713. https://doi.org/10.1115/1.2920939.
17. Yang, P.; Qu, S.; Chang, Q.; Guo, F. On the Theory of Thermal Elastohydrodynamic Lubrication at High Slide-Roll Ratios—Line Contact Solution. *J. Tribol.* **2001**, *123*, 36–41. https://doi.org/10.1115/1.1330738.

18. Rong-Tsong, L.; Chao-Ho, H. A fast method for the analysis of thermal-elastohydrodynamic lubrication of rolling/sliding line contacts. *Wear* **1993**, *166*, 107–117. https://doi.org/10.1016/0043-1648(93)90285-T.
19. Kim, K.H.; Sadeghi, F. Non-Newtonian Elastohydrodynamic Lubrication of Point Contact. *J. Tribol.* **1991**, *113*, 703–711. https://doi.org/10.1115/1.2920682.
20. Bair, S.S. *High Pressure Rheology for Quantitative Elastohydrodynamics*, 2nd ed.; Elsevier: Amsterdam, The Netherlands, 2019.
21. Eyring, H. Viscosity, Plasticity, and Diffusion as Examples of Absolute Reaction Rates. *J. Chem. Phys.* **1936**, *4*, 283–291. https://doi.org/10.1063/1.1749836.
22. Bair, S.; Habchi, W. Effects of a typical shear dependent viscosity on analytical elastohydrodynamic lubrication film thickness predictions: A critical issue for the classical approach. *Proc. Inst. Mech. Eng. Part J J. Eng. Tribol.* **2024**, *238*, 521–528. https://doi.org/10.1177/13506501231224005.
23. Bair, S. Actual Eyring models for thixotropy and shear-thinning: Experimental validation and application to EHD. *J. Tribol.* **2004**, *126*, 728–732. https://doi.org/10.1115/1.1792693.
24. Tošić, M.; Larsson, R.; Lohner, T. Thermal Effects in Slender EHL Contacts. *Lubricants* **2022**, *10*, 89. https://doi.org/10.3390/lubricants10050089.
25. Hartinger, M.; Reddyhoff, T. CFD modeling compared to temperature and friction measurements of an EHL line contact. *Tribol. Int.* **2018**, *126*, 144–152. https://doi.org/10.1016/j.triboint.2018.05.012.
26. Havaej, P.; Degroote, J.; Fauconnier, D. Sensitivity of TEHL Simulations to the Use of Different Models for the Constitutive Behaviour of Lubricants. *Lubricants* **2023**, *11*, 151. https://doi.org/10.3390/lubricants11030151.
27. Yasutomi, S.; Bair, S.; Winer, W.O. An Application of a Free Volume Model to Lubricant Rheology I—Dependence of Viscosity on Temperature and Pressure. *J. Tribol.-Trans. ASME* **1984**, *106*, 291–301. https://doi.org/10.1115/1.3260907.
28. Bair, S.; Mary, C.; Bouscharain, N.; Vergne, P. An improved Yasutomi correlation for viscosity at high pressure. *Proc. Inst. Mech. Eng. Part J J. Eng. Tribol.* **2013**, *227*, 1056–1060. https://doi.org/10.1177/1350650112474394.
29. Ree, T.; Eyring, H. Theory of Non-Newtonian Flow. II. Solution System of High Polymers. *J. Appl. Phys.* **1955**, *26*, 800–809. https://doi.org/10.1063/1.1722099.
30. Carreau, P.J. Rheological Equations from Molecular Network Theories. *Trans. Soc. Rheol.* **1972**, *16*, 99–127. https://doi.org/10.1122/1.549276.
31. Mawatari, T. Recent Trends in EHL Numerical Analysis Applying Shear-Thinning Models. *J. Jpn. Soc. Tribol.* **2021**, *66*, 91–97. https://doi.org/10.18914/tribologist.66.02_91.
32. Li, W.; Jadhao, V. Comparing Phenomenological Models of Shear Thinning of Alkanes at Low and High Newtonian Viscosities. *Tribol. Lett.* **2024**, *72*, 112. https://doi.org/10.1007/s11249-024-01908-7.
33. Hopper, N.; Bennett, D.W.; Espinosa-Marzal, R.M.; Tysoe, W. Shear Thinning and Stress-Dependent Viscosity Activation Volumes: Combining Eyring and Carreau. *Tribol. Lett.* **2025**, *73*, 108. https://doi.org/10.1007/s11249-025-02047-3.
34. Ardah, S.; Profito, F.J.; Dini, D. A comprehensive review and trends in lubrication modelling. *Adv. Colloid Interface Sci.* **2025**, *342*, 103492. https://doi.org/10.1016/j.cis.2025.103492.
35. Katyal, P.; Kumar, P. Central film thickness formula for shear thinning lubricants in EHL point contacts under pure rolling. *Tribol. Int.* **2012**, *48*, 113–121. https://doi.org/10.1016/j.triboint.2011.11.007.
36. He, Z.; Wang, X.; Li, Y.; Yang, Y. Analysis of Gear System Dynamics Based on Thermal Elastohydrodynamic Lubrication Effects. *Lubricants* **2025**, *13*, 411. https://doi.org/10.3390/lubricants13090411.
37. Echávarri Otero, J.; de la Guerra Ochoa, E.; Chacón Tanarro, E.; Díaz Lantada, A.; Munoz-Guijosa, J.M. Analytical model for predicting friction in line contacts. *Lubr. Sci.* **2016**, *28*, 189–205. https://doi.org/10.1002/ls.1325.
38. de la Guerra Ochoa, E.; Echávarri Otero, J.; Sánchez López, A.; Chacón Tanarro, E.; del Río, L.ó.pez B. Film Thickness Formula for Thermal EHL Line Contact Considering a New Reynolds–Carreau Equation. *Tribol. Lett.* **2018**, *66*, 31. https://doi.org/10.1007/s11249-018-0981-6.
39. Bruyere, V.; Fillot, N.; Morales-Espejel, G.E.; Vergne, P. Computational fluid dynamics and full elasticity model for sliding line thermal elastohydrodynamic contacts. *Tribol. Int.* **2012**, *46*, 3–13. https://doi.org/10.1016/j.triboint.2011.04.013.
40. Hamrock, B.J.; Schmid, S.R.; Jacobson, B.O. *Fundamentals of Fluid Film Lubrication*; CRC Press: Boca Raton, FL, USA, 2004. https://doi.org/10.1201/9780203021187.
41. Hajishafiee, A.; Kadiric, A.; Ioannides, S.; Dini, D. A coupled finite-volume CFD solver for two-dimensional elasto-hydrodynamic lubrication problems with particular application to rolling element bearings. *Tribol. Int.* **2017**, *109*, 258–273. https://doi.org/10.1016/j.triboint.2016.12.046.

42. Lee, D. Exploring Elastohydrodynamic Lubrication Using Finite-Volume Computational Modelling Techniques. Ph.D. Thesis, Imperial College London, London, UK, 2019. https://doi.org/10.25560/81590.
43. Peterson, W.; Singh, K.; Sadeghi, F. Fluid–Solid Interaction Modeling of Elastohydrodynamic Lubrication Point Contacts. *J. Tribol.* **2022**, *144*, 111601. https://doi.org/10.1115/1.4054589.
44. Singh, K.; Sadeghi, F.; Peterson, W.; Lorenz, S.J.; Villarreal, J.; Jinmon, T. A CFD-FEM based partitioned fluid structure interaction model to investigate surface cracks in elastohydrodynamic lubricated line contacts. *Tribol. Int.* **2022**, *171*, 107532. https://doi.org/10.1016/j.triboint.2022.107532.
45. Kaneta, M.; Cui, J.; Yang, P.; Krupka, I.; Hartl, M. Influence of thermal conductivity of contact bodies on perturbed film caused by a ridge and groove in point EHL contacts. *Tribol. Int.* **2016**, *100*, 84–98. https://doi.org/10.1016/J.TRIBOINT.2015.11.022.
46. Yang, P.; Wang, J.; Kaneta, M. Thermal and non-Newtonian numerical analyses for starved EHL line contacts. *J. Tribol.* **2006**, *128*, 282–290. https://doi.org/10.1115/1.2164465.
47. Ehret, P.; Dowson, D.; Taylor, C.M. On lubricant transport conditions in elastohydrodynamic conjunctions. *Proc. R. Soc. Lond. Ser. A Math. Phys. Eng. Sci.* **1998**, *454*, 763–787. https://doi.org/10.1098/rspa.1998.0185.
48. Blazek, J. *Computational Fluid Dynamics: Principles and Applications*; Elsevier: Amsterdam, The Netherlands, 2015. https://doi.org/10.1016/C2013-0-19038-1.
49. Batina, J.T. Unsteady Euler airfoil solutions using unstructured dynamic meshes. *AIAA J.* **1990**, *28*, 1381–1388. https://doi.org/10.2514/3.25229.
50. Roelands, C.J.A. Correlational Aspects of the Viscosity-Temperature-Pressure Relationship of Lubricating Oils. Ph.D. Thesis, Technical University of Delft, Delft, The Netherlands, 1966.
51. Chu, X.; Chen, F.; Wang, J. Lubrication Characteristics and Thermal Behavior of Non-Orthogonal Face Gear Pairs in Point Contact. *Lubricants* **2025**, *14*, 9. https://doi.org/10.3390/lubricants14010009.
52. Farrenkopf, F.; Lohner, T.; Stahl, K. Mixed and thermal elastohydrodynamic simulation of cylindrical gear designs. *Forsch. Ingenieurwes* **2025**, *89*, 127. https://doi.org/10.1007/s10010-025-00882-3. Erratum in *Forsch. Ingenieurwes* **2025**, *89*, 155.
53. Neupert, T.; Bartel, D. Evaluation of Various Shear-Thinning Models for Squalane Using Traction Measurements, TEHD and NEMD Simulations. *Lubricants* **2023**, *11*, 178. https://doi.org/10.3390/lubricants11040178.
54. Lu, R.; Tang, W.; Huang, Q.; Xie, J. An Improved Load Distribution Model for Gear Transmission in Thermal Elastohydrodynamic Lubrication. *Lubricants* **2023**, *11*, 177. https://doi.org/10.3390/lubricants11040177.
55. Simpson, M.; Rahmani, R.; Dolatabadi, N.; Morris, N.; Jones, D.; Craig, C. An analytical friction model for point contacts subject to boundary and mixed elastohydrodynamic lubrication. *Tribol. Int.* **2024**, *196*, 109699. https://doi.org/10.1016/j.triboint.2024.109699.
56. Liu, X.; Long, T.; Li, X.; Guo, F. Thermal EHL analysis of the inner ring rib and roller end in tapered roller bearings with the Carreau model. *Front. Manuf. Technol.* **2023**, *2*, 1029860. https://doi.org/10.3389/fmtec.2022.1029860.
57. Liu, H.C.; Zhang BBin Schneider, V.; Venner, C.H.; Poll, G. Two-dimensional generalized non-Newtonian EHL lubrication: Shear rate-based solution versus shear stress-based solution. *Proc. Inst. Mech. Eng. Part J J. Eng. Tribol.* **2021**, *235*, 2626–2639. https://doi.org/10.1177/13506501211050484.
58. Bair, S.; Casalini, R. A Scaling Parameter and Function for the Accurate Correlation of Viscosity With Temperature and Pressure Across Eight Orders of Magnitude of Viscosity. *J. Tribol.* **2008**, *130*, 041802. https://doi.org/10.1115/1.2959116.
59. Habchi, W.; Vergne, P.; Bair, S.; Andersson, O.; Eyheramendy, D.; Morales-Espejel, G.E. Influence of pressure and temperature dependence of thermal properties of a lubricant on the behaviour of circular TEHD contacts. *Tribol. Int.* **2010**, *43*, 1842–1850. https://doi.org/10.1016/j.triboint.2009.10.002.
60. Schnerr, G.; Sauer, J. Physical and numerical modeling of unsteady cavitation dynamics. In Proceedings of the ICMF-2001, 4th International Conference on Multiphase Flow, New Orleans, LA, USA, 27 May–1 June 2001.
61. Kaneta, M.; Shigeta, T.; Yang, P. Effects of Compressive Heating on Traction Force and Film Thickness in Point EHL Contacts. *J. Tribol.* **2005**, *127*, 435–442. https://doi.org/10.1115/1.1843153.
62. Habchi, W.; Vergne, P. On the compressive heating/cooling mechanism in thermal elastohydrodynamic lubricated contacts. *Tribol. Int.* **2015**, *88*, 143–152. https://doi.org/10.1016/j.triboint.2015.03.025.
63. Reddyhoff, T.; Spikes, H.A.; Olver, A.V. Compression Heating and Cooling in Elastohydrodynamic Contacts. *Tribol. Lett.* **2009**, *36*, 69–80. https://doi.org/10.1007/s11249-009-9461-3.
64. Habchi, W. *Finite Element Modelling of Elastohydrodynamic Lubrication Problems*; Wiley: Hoboken, NJ, USA, 2018. https://doi.org/10.1002/9781119225133.
65. Dowson, D.; Higginson, G.R. *Elastohydrodynamic Lubrication*; Pergamon Press: Oxford, UK, 1977.

66. Carslaw, H.S.; Jaeger, J.C. *Conduction of Heat in Solids*, 2nd ed.; Oxford Science Pub.: Oxford, UK, 1959.
67. Jaeger, J.C. Moving sources of heat and the temperature at sliding contacts. *J. Proc. R. Soc. New South Wales* **1942**, *76*, 203.
68. Reddy, J.N. *An Introduction to Continuum Mechanics*, 2nd ed.; Cambridge University Press: Cambridge, UK, 2013. https://doi.org/10.1017/CBO9781139178952.
69. Habchi, W.; Eyheramendy, D.; Vergne, P.; Morales-Espejel, G. A Full-System Approach of the Elastohydrodynamic Line/Point Contact Problem. *J. Tribol.* **2008**, *130*, 021501. https://doi.org/10.1115/1.2842246.
70. Hartinger, M.; Dumont, M.-L.; Ioannides, S.; Gosman, D.; Spikes, H. CFD Modeling of a Thermal and Shear-Thinning Elastohydrodynamic Line Contact. *J. Tribol.* **2008**, *130*, 041503. https://doi.org/10.1115/1.2958077.
71. Singh, K.; Sadeghi, F.; Russell, T.; Lorenz, S.J.; Peterson, W.; Villarreal, J.; Jinmon, T. Fluid–Structure Interaction Modeling of Elastohydrodynamically Lubricated Line Contacts. *J. Tribol.* **2021**, *143*, 091602. https://doi.org/10.1115/1.4049260.

**Disclaimer/Publisher's Note:** The statements, opinions and data contained in all publications are solely those of the individual author(s) and contributor(s) and not of MDPI and/or the editor(s). MDPI and/or the editor(s) disclaim responsibility for any injury to people or property resulting from any ideas, methods, instructions or products referred to in the content.